Generation of Low-Frequency Unstable Modes in a Coupled Equatorial Troposphere and Ocean Mixed-Layer Model

P. C. CHU

Department of Oceanography, Naval Postgraduate School, Monterey, California

(Manuscript received 18 June 1991, in final form 12 May 1992)

ABSTRACT

An important issue presented here is the existence of two different types of correlation between time rate of change of sea surface temperature (SST) $\partial T_s/\partial t$ and the ocean mixed-layer (OML) depth h_w, depending on the ocean surface conditions. In the tropics, the net heat flux (including radiation budget) at the ocean surface is generally downward and dampens the OML turbulent kinetic energy (TKE). As the ocean surface is under weak wind forcing, the OML shallows to the Monin–Obukhov length scale due to insufficient wind-generated TKE to entrain the deep cool water into the OML. Net heat gain at the ocean surface and very little heat loss at the OML base leads to a warming OML. The thinner the OML, the warmer the OML. Therefore, $\partial T_s/\partial t$ and h_w are negatively correlated; however, as the ocean surface is under strong wind forcing, the OML deepens due to sufficient wind-generated TKE to entrain the deep cool water into OML. The excessive heat loss at the OML base (entrainment heat flux) over net heat gain at the ocean surface leads to a cooling OML. The thicker the OML, the warmer the OML. Therefore, $\partial T_s/\partial t$ and h_w are positively correlated. The shift of positive-only correlation between $\partial T_s/\partial t$ and h_w (as conventionally thought to be), to two-way correlation leads to a new theory about the interannual tropical ocean–atmosphere interaction.

To investigate the impact of this new idea on the interannual tropical ocean–atmosphere interaction, an Air–Ocean Surface Heat Exchange (AOSHE) Model, which is a coupled system consisting of the Wind-Induced Surface Heat Exchange (WISHE) Model (Yano and Emanuel) and the Ocean Mixed-Layer (OML) Model (Chu and Garwood) has been developed. The major advantage of the AOSHE model is simple but contains realistic thermodynamics in both ocean and atmosphere. The SST, predicted by the OML model, largely affects the surface evaporation rate, which in turn impacts on the atmosphere. On the other hand, the surface wind stress and buoyancy flux, predicted by the WISHE model, drives the ocean mixed layer. Two different types of low-frequency (interannual) modes are found in the AOSHE model for different ocean surface conditions. For weak surface wind forcing, the low-frequency mode (called AOSHE W-mode) propagates westward with phase speed around 20 cm s^{-1}, and maximum growth rate 2.2 yr^{-1}. The growth rate increases as the wavenumber decreases. The most unstable mode is at the lowest wavenumber with periods of 2–10 years. For strong surface wind forcing, however, the low-frequency mode (called AOSHE S-mode) propagates eastward with phase speed 10–100 cm s^{-1} and period 1–3 years. This low-frequency mode has strong wavelength selection. The maximum growth rate (nearly 0.5 yr^{-1}) appears at the 3–5 zonal wavenumber.

1. Introduction

The phenomenon of El Niño and Southern Oscillation (ENSO) exhibits a time scale of 2–9 years. Two complementary phases (La Niña and El Niño) of the Southern Oscillation are defined by Philander (1985). Several important mechanisms (virtually wave-type) of air–ocean interaction for the ENSO phenomenon have been developed in the past decade: the slow propagation of oceanic Rossby and Kelvin waves across the Pacific Ocean (e.g., McCreary 1983; Battisti 1988; Battisti and Hirst 1989; Cane et al. 1990; Graham and White 1991); the generation of two states—El Niño and La Niña (e.g., McCreary and Anderson 1984); and air–ocean coupled instability (e.g., Hirst 1986; Rennick and Haney 1986; Yamagata 1985; Zebiak and Cane 1987; Kuo 1989). Despite the recent debate between Graham and White (1991) and Battisti (1991) on the role of off-equatorial oceanic Rossby waves during ENSO, and despite some speculations on ENSO events triggered by high-frequency (30–60 day) oscillations (e.g., Lau and Chan 1986; Lau and Shen 1988; and Hirst and Lau 1990), the ENSO oscillations are usually thought to be driven by delayed negative feedback due to reflected oceanic Rossby wave activity, aspects which can be traced through Wyrtki (1975), McCreary (1983), Cane and Zebiak (1985), and Battisti (1988, 1989) among others. These models, however, involve two major assumptions: (a) SST perturbation or the time rate of change of SST perturbation is positively correlated to the perturbation of upper-ocean thickness (the thicker the upper-ocean layer, the higher the SST); (b) surface winds over the eastern Pacific are switched from equatorial easterlies repre-

Corresponding author address: Dr. P. C. Chu, Naval Postgraduate School, Department of Oceanography, Code OC/CU, Monterey, CA 93943-5100.

senting Walker circulation when the eastern Pacific is cool (La Niña) to extra-equatorial (off-equatorial) easterlies representing enhanced Hadley circulation when the eastern Pacific is warm (El Niño). This was presented by Bjerknes (1966, 1969) and later pursued in numerical models by McCreary (1983), Zebiak and Cane (1987), and Battisti (1988, 1989). These are the wave-type ENSO theories.

Recently, a SST-type ENSO theory was presented by Neelin (1991). The new idea brought to the community is the separation of the slow SST mode and the (relatively fast) modified oceanic wave modes. Within the SST mode, the ocean dynamics tends to come into balance quickly on the interannual time scales over which SST is evolving. Neelin (1991) further argues that it is the slow SST mode rather than the time delay associated with oceanic wave propagation across the basin that is essential to the existence of interannual coupled oscillations. If Neelin's conclusion is correct, the thermodynamics in ocean and atmosphere should play a key role in determining the SST mode. In Neelin's model, the ocean component is based on a modified shallow-water model with a fixed-depth mixed layer. The SST equation contains advection (both horizontal and vertical) and a Newtonian cooling term representing all one-dimensional vertical processes: mixing, sea surface sensible and latent heat fluxes, long- and shortwave radiation. The atmospheric part is a functional relationship between the surface wind stress and SST. In the real ocean, the OML depth has large temporal and spatial variations, and the one-dimensional vertical processes are too complicated to be interpreted as a Newtonian cooling term. The atmospheric thermodynamics is also too simple to be realistic for the problems for which thermodynamical processes are important. Therefore, the question may arise: What is the behavior of the SST mode in a more thermodynamically realistic coupled system?

For the atmospheric thermodynamics in most ENSO models it is simply assumed that evaporation from the ocean surface is immediately reflected as heating of the atmosphere, which implies upward velocity everywhere in the atmosphere. In investigating the linkage between the 40–50-day oscillation and ENSO (Lau and Shen 1988), the atmospheric thermodynamics is improved by expressing precipitation as the sum of surface evaporation and moisture convergence. Their study shows the importance of moist processes 1) in generation of eastward-propagating unstable modes on an intraseasonal time scale (30–50 days) and 2) possibly to onset and evolution of ENSO-like events in the tropical atmosphere–ocean system. A coupled air–ocean system with an atmospheric part from the Lau and Shen (1988) model and an oceanic part from the Hirst (1986) model was developed (Hirst and Lau 1990) to determine the relationship between the intraseasonal and interannual oscillations. The Hirst and Lau model results emphasize the importance of including prognostic atmospheric equations in simple, coupled ocean–atmosphere models. The atmospheric part of the Lau and Shen (1988) and Hirst and Lau (1990) models and any other simple, coupled models still imply an assumption that vertical velocity in the atmosphere is upward everywhere, such that moisture evaporated from the ocean surface can directly warm the atmosphere. The oceanic part of the Hirst (1986) and Hirst and Lau (1990) models contains an OML in one of the two regimes (to be discussed in detail in section 2).

Schopf and Suarez (1988) proposed a coupled dry atmosphere and embedded mixed layer–ocean circulation model for simulating ENSO-like variability. The model predicts some incorrect results; that is, the ocean mixed layer is cooler than surface air over most of the tropical ocean basin (model climatology). Several decades ago, meteorologists were already aware of the fact that the largest part of the tropical oceans appears to be slightly warmer—near 0.5°C on the average—than the surface air, both in the annual mean and seasonal breakdowns (Riehl 1954). Recent analysis (Hsiung 1986) from a comprehensive dataset covering the global ocean surface for a period from 1946 to 1979 provided by Fleet Numerical Oceanographic Center also shows similar results: the tropical ocean is warmer (0.1°–0.9°) than surface air. Two flaws in the Schopf–Suarez model (1988) cause this discrepancy: 1) the thermodynamics is improperly parameterized so that the atmosphere is thermally driven by both radiation (Newtonian "*cooling*" form) and air–ocean interfacial heat flux, but the ocean is thermally forced only by the interfacial heat flux; and 2) wind stress is used in two contradictory ways: surface shear production S (wrong dimension used by Schopf and Suarez 1988) is used as a constant in ocean surface TKE production and as a variable (proportional to the lower-layer wind velocity) in ocean surface current generation. Furthermore, even the Coriolis force has the wrong sign in the ocean model. In fact, observations show that incoming solar radiation and latent heat flux are the two dominant components controlling net surface energy fluxes (Hsiung 1986), that is, the tropical ocean is mainly heated by solar radiation and cooled by evaporation. Heat gain in the OML is not the same as the heat loss from the atmosphere. Absence of solar radiation in the ocean part of the Schopf–Suarez model leads to this unrealistic result that the OML is cooler than the surface air over most of the tropical ocean basin. Moreover, the assumed constant ocean surface turbulent production by wind mixing (1.25×10^{-6} m^3 s^{-3}), corresponding to a rather strong surface wind ($\sim$10 m s^{-1}), excludes the effect of weak surface winds on OML dynamics, and the effects of surface wind variation on thermodynamics of the atmosphere (wind–evaporation feedback, e.g., Emanuel 1987) and oceans (wind–OML feedback).

Therefore, to investigate the SST mode, more realistic thermodynamics in both ocean and atmosphere

are needed. The SST mode is further investigated in this research by a coupled model with more realistic thermodynamics in both atmosphere and ocean: the Air–Ocean Surface Heat Exchange (AOSHE) Model, which is a coupled system consisting of the Wind-Induced Surface Heat Exchange (WISHE) Model (Yano and Emanuel 1991; hereafter YE91), and the OML model (Chu et al. 1990; hereafter CGM90; Chu and Garwood 1991; hereafter CG91).

2. AOSHE Model

Figure 1 presents a schematic view of the coupled WISHE and OML model (the AOSHE Model). Above the air–ocean interface, it is the ordinary WISHE Model depicted by E87 and YE91. Below the air–ocean interface, it is the OML Model described by CGM90 and CG91, which is a modified Kraus and Turner (1967) model. The fluxes across the interface are no longer fixed and drive motions in both atmosphere and ocean.

a. An OML switcher

Arguments are cast in terms of simple mixed-layer models (Chu et al. 1990; Chu and Garwood 1991), where it is assumed that the temperature and velocity are uniform over some depth h_w, the thickness of the OML, and that the penetration depth of solar radiation is much smaller than h_w. With these assumptions, one can write

$$\frac{\partial T_s}{\partial t} + \mathbf{u}_w \cdot \nabla T_s = \frac{Q_0 - \Lambda_w(\Pi) Q_{-h}}{\rho_{w0} c_{pw} h_w}, \tag{1}$$

where T_s is the SST, $\mathbf{u}_w$ is the horizontal velocity, ρ_{w0} is the characteristic seawater density, c_{pw} is the seawater specific heat under constant pressure, Q_0 is the net surface heat flux with downward being positive, $\Lambda_w(\Pi)$ is the Heaviside step function of Π, and Π is defined by

$$\Pi \equiv C_1 u_{w*}^3 - C_2 \alpha g h_w Q_0 / \rho_{w0} c_{pw}, \tag{2}$$

denoting surface forcing condition. Here C_1 and C_2 are tuning coefficients, α is the thermal expansion coefficient,

$$u_{w*} \equiv (C_D \rho_{a0} / \rho_{w0})^{1/2} |\mathbf{V}_b| \tag{3}$$

is the water surface friction velocity, and $|\mathbf{V}_b|$ is the subcloud-layer wind speed; Q_{-h} is the entrainment heat flux at the base of the OML:

$$\frac{Q_{-h}}{\rho_{w0} c_{pw}} = w_e (T_s - T_{-h}), \tag{4}$$

where w_e and T_{-h} are the entrainment velocity and the temperature at the base of the OML.

Entrainment velocity can also be parameterized in terms of OML turbulent kinetic energy (TKE) balance. Since salinity effects are not considered at present, sources and sinks of TKE at ocean surface are wind work (proportional to wind speed cubed) and buoyant damping (forcing) due to surface warming (cooling). This is given by

$$w_e = \frac{\Pi}{g h_w \alpha (T_s - T_{-h})}. \tag{5}$$

The step function Λ_w acts as an OML switcher.

The value of Λ_w is 1 for $\Pi > 0$, which is usually associated with strong surface wind forcing in tropics ($Q_0 > 0$). The heat equation (1) for the entrainment regime becomes

$$\frac{\partial T_s}{\partial t} + \mathbf{u}_w \cdot \nabla T_s = - \frac{Q_{-h} - Q_0}{\rho_{w0} c_{pw} h_w}. \tag{6a}$$

In this case, the wind-generated TKE is strong enough to entrain the deep cooler water into the OML. The heat loss at the OML base, that is, the entrainment heat flux (Q_{-h}), is larger than the heat gain at the ocean surface: $Q_{-h} > Q_0$ (Miller 1976), which makes the OML a cooling layer. As shown in (6a), an increase in the OML thickness h_w leads to an increase of $\partial T_s / \partial t$, which implies a *positive correlation* between $\partial T_s / \partial t$ and h_w. The entrainment rate is determined by (5) and is substituted into the following equation to prognosticate the mixed-layer depth h_w:

$$\frac{\partial h_w}{\partial t} = w_e - w_{-h}. \tag{7a}$$

Here w_{-h} is the vertical velocity at the mixed-layer base caused by Ekman pumping or by the ocean interior dynamical processes. Another way to view (7a) is that the entrainment velocity w_e is the summation of the vertical velocity at the OML base w_{-h} and the time rate change of OML thickness $\partial h_w / \partial t$. The vertical thermal advection in OML base becomes part of the heat flux Q_{-h} through (4).

The value of Λ_w is 0 for $\Pi \leqslant 0$, which is usually associated with weak surface wind forcing in the tropics. In this case, the wind generated TKE is so weak that it is unable to entrain the deep cooler water into the OML ($Q_{-h} = 0$). The OML then shoals to the Monin–Obukhov length scale. The heat equation (1) for the shallowing regime becomes

$$\frac{\partial T_s}{\partial t} + \mathbf{u}_w \cdot \nabla T_s = \frac{Q_0}{\rho_{w0} c_{pw} h_w}. \tag{6b}$$

The mixed-layer depth is calculated from a balance of the remaining terms in (5), and it equals the Monin–Obukhov length scale l_w:

$$l_w = \frac{C_1 u_{w*}^3}{C_2 \alpha g Q_0 / \rho_{w0} c_{pw}}. \tag{7b}$$

Absence of vertical advection in heat equation (6b) for the weak surface wind-forcing case ($\Lambda_w = 0$) is due to the small cooling rate caused by vertical advection. The Ekman layer thickness, $\delta_E = (2K/|f|)^{1/2}$, in-

creases equatorward and tends to infinity at the equator. Here, K is the eddy viscosity. Therefore, near the equator, δ_E should be much larger than the Monin–Obukhov length scale, which is nearly 20 m in the equatorial Pacific (Schneider and Muller 1990). The upwelling velocity at the base of the equatorial Ekman layer is nearly 1 m day^{-1} (Wyrtki 1981) and decreases upward. Therefore, the vertical velocity in the OML under weak surface wind forcing is only a fraction of the vertical velocity at the base of the Ekman layer. The value of 0.1 m day^{-1} might be a reasonable estimation. Furthermore, the temperature jump at the OML base $T_s - T_{-h}$ is on the order of 3°C or less, and the net ocean surface heating at the equatorial Pacific Q_0 is nearly 100 W m^{-2} (Wyrtki 1981). The heating rate caused by the ocean surface warming is estimated by $Q_0/\rho_{w0}c_{pw}h_w \approx 0.052$°C day^{-1}. The cooling rate caused by the vertical advection, however, is estimated by $-w_{-h}(T_s - T_{-h})/h_w \approx -0.015$°C day^{-1}, which is much smaller than the surface heating rate. Therefore, it is reasonable to consider the OML under weak surface wind forcing as a warming layer. An increase in the OML thickness h_w leads to a decrease of $\partial T_s/\partial t$, which implies a *negative correlation* between $\partial T_s/\partial t$ and h_w.

We should point out here that the OML model only depicts local thermal processes; no large-scale ocean dynamical processes are involved. This is reasonable only when the ocean dynamics is assumed to come quickly into balance on an interannual time scale over which the SST is evolving (Neelin 1991). If we want to know both the slow SST mode and the relatively fast modified ocean wave modes or if we want to improve the ENSO prediction model, we need an embedded mixed layer–ocean circulation model. In this paper, (5), (6), and (7) are base equations of OML Model.

b. *WISHE Model*

WISHE is a multilayer model, in which the troposphere is divided into a free troposphere and a subcloud layer. Two good reasons for us to choose WISHE as the atmospheric part are 1) realistic thermodynamics (especially the treatment of cumulus clouds with shallow updraft–downdraft couplet) for the investigation of the SST mode and 2) it is still simple for numerical and analytical studies. The coordinate system is chosen on the equatorial β plane with x in zonal, y in latitudinal, and z in vertical. The subgrid-scale motions are divided into the deep cumulus convective area and the quiescent surrounding environment. In addition to the deep convective updraft, a shallow updraft–downdraft couplet with equal updraft and downdraft mass fluxes is also included (Fig. 1).

The subcloud layer of thickness h obtains moist entropy from the ocean by water vapor evaporation, while it loses moist entropy to the lower troposphere both by cloudy downdraft and by net subsidence within the surrounding environment. The free troposphere with thickness H obtains moist entropy from the subcloud

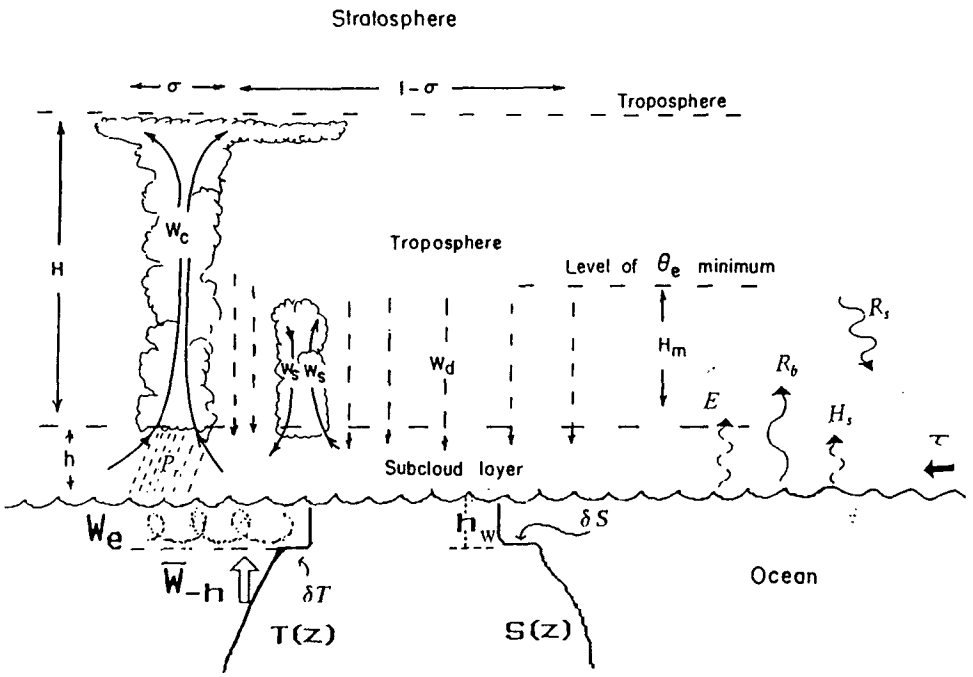

FIG. 1. Schematic presentation of the AOSHE model.

layer by shallow updrafts and from aloft by downward entropy advection, and loses by net radiative cooling (Fig. 2). Neglecting the local rate of temperature change inside clouds, the following set of equations are given by (YE91):

$$h\frac{d}{dt}(\ln\theta_{eb}) = C_\theta|\mathbf{V}_b|(\ln\theta_{es} - \ln\theta_{eb}) - \sigma_s w_s(\ln\theta_{eb} - \ln\theta_{em}) + (1-\sigma)w_d(\ln\theta_{eb} - \ln\theta_{em}), \quad (8a)$$

which is the moist entropy balance within the subcloud layer with thickness h,

$$H\frac{d}{dt}(\ln\theta_{em}) = -HR + \sigma_s w_s(\ln\theta_{eb} - \ln\theta_{em}) - (1-\sigma)w_d(\ln\theta_{eb} - \ln\theta_{em}), \quad (8b)$$

which is the entropy balance within the free troposphere with thickness H,

$$g\frac{d}{dt}(\ln\theta) = -N^2(1-\sigma)w_d - gR, \quad (8c)$$

which is the conservation of dry entropy in the free troposphere,

$$\nabla\cdot\mathbf{V}_b + H_m^{-1}[(1-\sigma)w_d + \sigma w_c] = 0, \quad (8d)$$

which is the continuity equation,

$$\frac{d\mathbf{V}_b}{dt} = -\nabla\delta\phi_b - \mathbf{k}\times\beta y\mathbf{V}_b - C_D h^{-1}|\mathbf{V}_b|\mathbf{V}_b, \quad (8e)$$

which is the momentum equation on an equatorial β plane,

$$\delta\ln\theta_{eb} = \frac{\Gamma_d}{\Gamma_m}\delta\ln\theta, \quad (8f)$$

which is the first supplementary relation obtained from assuming the equality of subcloud layer and midtropospheric moist entropy fluctuations (YE91), and

$$\delta\phi_b = -c_{pa}T_b\bar{\epsilon}\delta\ln\theta_{eb} + \overline{\delta\phi}, \quad (8g)$$

which is the second supplementary relation obtained by vertically integrating the hydrostatic relation.

Here, $\ln\theta_{eb}$ is the moist entropy in the subcloud layer; $\ln\theta_{em}$ the pressure-weighted mean of moist entropy through the depth of the troposphere; $\ln\theta_{es}$ the saturated moist entropy of the ocean surface; θ the potential temperature in the subcloud layer; $\mathbf{V}_b$ the horizontal velocity in the subcloud layer; and $\delta\phi_b$ the fluctuating component of geopotential in the subcloud layer. The vertical velocity of the deep cumulus convective area and the quiescent surrounding environment are w_c and w_d, respectively; σ is the fractional areal coverage of cumulus convection. In addition to the deep convective updrafts, a shallow updraft–downdraft couplet with equal updraft–downdraft mass fluxes is considered. The mass flux in the updraft and downdraft are denoted by $\sigma_s w_s$ and $-\sigma_s w_s$; H is the thickness of free troposphere; H_m is taken as the height of the level where the equivalent potential temperature θ_e is a minimum (see Fig. 2); h is the thickness of subcloud layer; N the Brunt–Väisälä frequency of the troposphere; R the net radiative cooling in the troposphere; and Γ_d and Γ_m

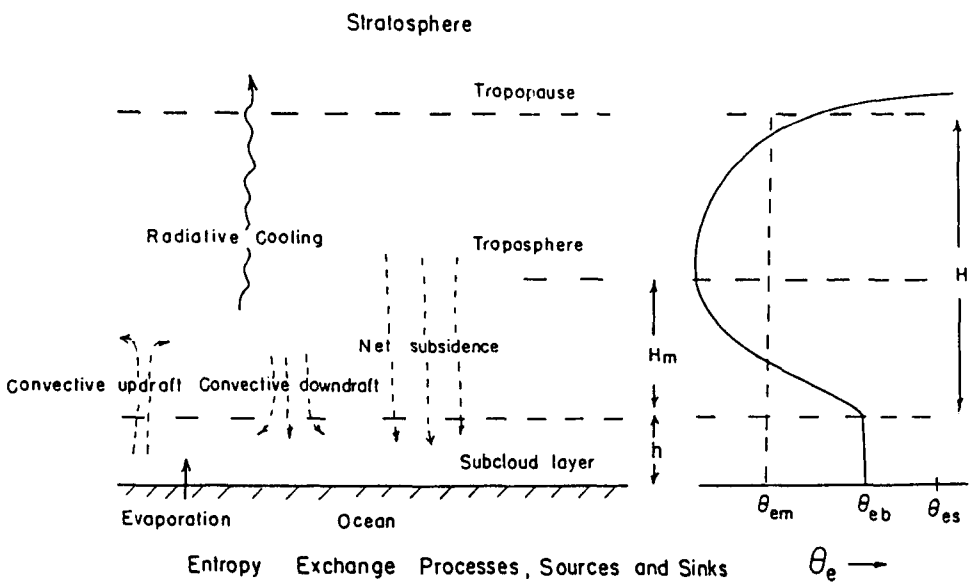

FIG. 2. Entropy exchange processes, sources, and sinks; mean entropy distribution (after Yano and Emanuel 1991).

are the moist and dry adiabatic lapse rates; c_{pa} is the atmospheric specific heat at constant pressure; and T and T_b are temperatures of the troposphere and the top of the subcloud layer, respectively. The overbar ($\bar{}$) in (8g) represents a mass-weighted tropospheric average, and

$$\bar{\epsilon} \equiv \frac{T_b - \bar{T}}{T_b}. \tag{9}$$

The precipitation efficiency of the WISHE model is simply defined as the ratio of the deep updraft mass flux to the total updraft mass flux:

$$\epsilon_p = \frac{\sigma w_c}{(\sigma w_c + \sigma_s w_s)}. \tag{10}$$

Solving for $\sigma_s w_s$ gives

$$\sigma_s w_s = \frac{(1 - \epsilon_p)}{\epsilon_p} \sigma w_c. \tag{11}$$

3. Ensemble means and perturbations

a. Basic state

All model variables are decomposed into two parts:

$$Z = \langle Z \rangle + Z',$$

where Z represents any AOSHE variable; $\langle Z \rangle$ and Z' denote ensemble mean and perturbation, respectively.

A basic state of the AOSHE model with constant zonal wind U is evaluated from the steady-state solutions for Eqs. (5), (6), and (7) of the OML and (8) of the WISHE (YE91). After some manipulations, the mean-state variables are given by

$$\frac{C_2\langle Q_0 \rangle}{\rho_{w0} c_{pw} \delta T} = \frac{C_1 \langle u_{w*} \rangle^3}{g\alpha \langle h_w \rangle \delta T} - \Lambda_w \langle w_e \rangle, \tag{12a}$$

$$\langle A_T \rangle = \frac{-\langle Q_0 \rangle}{\rho_{w0} c_{pw} \langle h_w \rangle} + \Lambda_w \frac{\langle w_e \rangle}{\langle h_w \rangle} \delta T, \tag{12b}$$

$$\langle w_e \rangle = \langle w_{-h} \rangle, \tag{12c}$$

$$\langle u_{w*} \rangle = \sqrt{C_D \rho_{a0}/\rho_{w0}}\, |U|, \tag{12d}$$

$$\langle \ln\theta_{eb} \rangle = \langle \ln\theta_{es} \rangle - \frac{H\langle R \rangle}{C_\theta |U|}, \tag{12e}$$

$$\langle \ln\theta_{em} \rangle = \langle \ln\theta_{eb} \rangle - \frac{\epsilon_p N^2 H}{g}, \tag{12f}$$

$$\langle w_c \rangle = \frac{g\langle R \rangle}{\sigma N^2}, \tag{12g}$$

$$\langle w_d \rangle = -\frac{g\langle R \rangle}{(1 - \sigma) N^2}, \tag{12h}$$

$$\langle R \rangle = C_\theta H^{-1} |U| \ln\left(\frac{\langle \theta_{es} \rangle}{\langle \theta_{eb} \rangle}\right). \tag{12i}$$

Note that a constant zonal wind U will lead to a constant zonal gradient of OML thickness (Philander 1990, p. 108). Therefore, the mean OML thickness $\langle h_w \rangle$ should be a linear function of x. When an easterly basic flow appears in the troposphere, the mean OML thickness $\langle h_w \rangle$ reduces eastward. In the present study, however, this zonal variation is absent. It is acceptable when we concentrate only on exploring the two-way correlation between temporal change in SST and mixed-layer depth perturbation and examining its effects on the behavior of the unstable mode in a coupled air–sea system. One should be very careful, however, when applying the current results to the whole Pacific basin.

When the AOSHE system is perturbed from its equilibrium state, the air–ocean feedback mechanism between the WISHE and the OML either causes the perturbation to grow (positive feedback) or to dampen (negative feedback). The principal purpose here is to study the SST mode in a more realistic thermodynamical coupled system. Hence, the energy exchange at the air–ocean interface is the primary focal point. Therefore, we shall neglect the perturbation of the temperature advection term (more related to wave mode) in OML A'_T. Hereafter, we omit the primes for perturbation variables.

b. Criterion for different surface conditions

After the decomposition and neglecting of the high-order terms, the continuity of momentum flux at the ocean surface (3) becomes:

$$\frac{u_{w*}}{\langle u_{w*} \rangle} = \frac{u_b}{|U|} \operatorname{sgn}(U), \tag{13}$$

which indicates that in the mean easterlies, east (or west) wind perturbation leads to the enhancement (or reduction) of TKE in OML; in the mean westerlies, otherwise is expected. The criterion for the different ocean surface conditions becomes

$$\langle l_w \rangle \left[1 + \frac{3u_b}{|U|} \operatorname{sgn}(U)\right] - \langle h_w \rangle \left(1 + \frac{Q_0}{\langle Q_0 \rangle}\right)\left(1 + \frac{h_w}{\langle h_w \rangle}\right) > 0 \tag{14a}$$

for the strong surface wind forcing, with the OML in the entrainment regime; and

$$\langle l_w \rangle \left[1 + \frac{3u_b}{|U|} \operatorname{sgn}(U)\right] - \langle h_w \rangle \left(1 + \frac{Q_0}{\langle Q_0 \rangle}\right)\left(1 + \frac{h_w}{\langle h_w \rangle}\right) < 0 \tag{14b}$$

for the weak surface wind forcing, with the OML retreating to the Monin–Obukhov length scale l_w. The surface wind and heat flux perturbations will change

the OML regime from one to the other. At the ocean surface, generally, the perturbation heat flux Q_0 is much smaller than the ensemble mean heat flux $\langle Q_0 \rangle$. The surface wind perturbation u_b will then take an important role to determine the OML regime since the background easterlies are rather weak ($|U| \sim 2$ m s^{-1}, YE91).

Four important processes change the surface heat flux: SST–surface heat flux feedback, wind–surface heat flux feedback, cloud–radiation feedback, and evaporation–surface heat flux feedback. Generally, SST–surface heat flux feedback and wind–surface heat flux feedback are treated as the most important thermal linkages between ocean and atmosphere in tropics. The perturbation–surface heat flux Q_0 is then approximately estimated by

$$Q_0 \approx -\rho_{a0} c_{pa} C_\theta [|U| T_s + \mathrm{sgn}(U) u_b (\langle \theta_{es} \rangle - \langle \theta_{eb} \rangle)], \quad (15a)$$

where C_θ is the ocean surface heat exchange coefficient; c_{pa} is the atmospheric specific heat at constant pressure (YE91). The deep water temperature perturbation T_{-h} is determined largely by the physical processes in the ocean interior and is assumed negligible in the present study. According to (4) the entrainment heat flux perturbation Q_{-h} is then computed by

$$Q_{-h} = \rho_{w0} c_{pw} (\langle w_{-h} \rangle T_s + w_e \delta T). \quad (15b)$$

c. *Perturbations in the OML model*

1) WEAK SURFACE WIND FORCING

During weak surface wind forcing, the OML depth is taken as the Monin–Obukhov length scale (7b), which is the algebraic equation for the three variables: h_w, u_{w*}, and Q_0. The fluctuation of the OML depth is caused by the perturbations of surface heat flux and the surface wind stress, that is,

$$\frac{h_w}{\langle h_w \rangle} = \frac{3u_{w*}}{\langle u_{w*} \rangle} - \frac{Q_0}{\langle Q_0 \rangle}. \quad (16)$$

The perturbation heat equation becomes

$$\frac{\partial T_s}{\partial t} = -\frac{1}{\tau_T} T_s - \frac{[3\langle Q_0 \rangle + \rho_{a0} c_{pa} C_\theta |U| (\langle \theta_{es} \rangle - \langle \theta_{eb} \rangle)]}{\rho_{w0} c_{pw} \langle h_w \rangle} \times \frac{u_b}{|U|} \mathrm{sgn}(U), \quad (17)$$

where τ_T^{-1} is thermal dissipation coefficient:

$$\tau_T \equiv \frac{\rho_{w0} c_{pw} \langle h_w \rangle}{2\rho_{a0} c_{pa} C_\theta |U|}. \quad (18)$$

2) STRONG SURFACE WIND FORCING

During strong surface wind forcing, the OML depth h_w satisfies the prognostic equation (7a). The Eqs. (5), (6a), and (7a) are used to obtain a single equation for SST perturbation. If the vertical velocity at the OML base w_{-h} is assumed to be determined by the dynamics of the ocean interior and not to be directly related to the surface heat exchange, the fluctuation of the OML depth for a strong surface wind forcing is caused by the perturbation of entrainment velocity w_e,

$$\frac{\partial h_w}{\partial t} = w_e. \quad (19)$$

The parameterization of w_e, Eq. (5), indicates that the perturbation entrainment velocity w_e is caused by the perturbations of the SST (T_s), the OML depth h_w, the surface water friction velocity u_{w*}, and the net surface heat flux Q_0,

$$w_e = -\langle w_e \rangle \frac{T_s}{\delta T} - \frac{C_2 Q_0}{\rho_{w0} c_{pw} \delta T} - \frac{C_1 \langle u_{w*} \rangle^3}{g\alpha \langle h_w \rangle \delta T} \left[\frac{h_w}{\langle h_w \rangle} - \frac{3u_b}{|U|} \mathrm{sgn}(U) \right]. \quad (20)$$

The local time rate change of perturbation SST is caused by perturbations of the OML thickness h_w, of the subcloud-layer zonal wind (through its effect on water surface friction velocity), and of surface heat flux Q_0. The SST perturbation equation for strong surface wind forcing becomes

$$\frac{\partial T_s}{\partial t} = -\frac{(1 + C_2)}{2} \tau_T^{-1} T_s + \left[-\frac{(1 - C_2)\langle Q_0 \rangle}{\rho_{w0} c_{pw} \langle h_w \rangle} + \frac{2\langle w_{-h} \rangle}{\langle h_w \rangle} \delta T \right] \frac{h_w}{\langle h_w \rangle} - \left[3\left(\frac{C_2 \langle Q_0 \rangle}{\rho_{w0} c_{pw} \langle h_w \rangle} + \frac{\langle w_{-h} \rangle}{\langle h_w \rangle} \delta T \right) + \frac{(1 + C_2)\rho_{a0} c_{pa} C_\theta |U| (\langle \theta_{es} \rangle - \langle \theta_{eb} \rangle)}{\rho_{w0} c_{pw} \langle h_w \rangle} \right] \frac{u_b}{|U|} \mathrm{sgn}(U). \quad (21)$$

Substitution of (15) and (20) into (19) leads to a prognostic equation for OML-depth perturbation:

$$\frac{\partial h_w}{\partial t} = \left(\frac{C_2}{2} \langle h_w \rangle \tau_T^{-1} - \langle w_{-h} \rangle \right) \frac{T_s}{\delta T} - \left(\frac{C_2 \langle Q_0 \rangle}{\rho_{w0} c_{pw} \delta T} + \langle w_{-h} \rangle \right) \frac{h_w}{\langle h_w \rangle} + \left[3\left(\frac{C_2 \langle Q_0 \rangle}{\rho_{w0} c_{pw} \delta T} + \langle w_{-h} \rangle \right) + \frac{C_2 \rho_{a0} c_{pa} C_\theta |U| (\langle \theta_{es} \rangle - \langle \theta_{eb} \rangle)}{\rho_{w0} c_{pw} \delta T} \right] \frac{u_b}{|U|} \mathrm{sgn}(U). \quad (22)$$

A relationship between SST perturbation T_s and surface wind perturbation U_b is obtained by elimination of OML-depth perturbation h_w from (21) and (22).

4. Air–ocean feedback mechanism

The tropical subcloud layer is usually dominated by mean easterlies. In the east (west) of the deep convective region, the surface wind speed is enhanced (reduced); therefore, the OML depth is increased (decreased). When the atmosphere and ocean are decoupled (WISHE model), the surface evaporation is always enhanced (reduced) in the east (west) of the initial convective region by the WISHE mechanism. When the atmosphere and ocean are coupled (AOSHE model), the time rate change of surface evaporation is also related to SST (called AOSHE mechanism) through the first term in the right-hand side of (8a). The AOSHE mechanism is different from the WISHE mechanism (e.g., enhanced surface evaporation always in the east of the convective region) in such a way that the surface evaporation in the AOSHE Model also depends on SST. Generally, the increase in SST augments the surface evaporation rate. The effect of surface wind and buoyancy forcing on SST is rather complicated, however. There are three cases available for the tropical oceans.

(i) *Weak mean easterlies and weak initial perturbations.* In this case, the total surface winds, which are the summation of the mean easterlies and the surface wind perturbation associated with the initial positive SST fluctuation, are weak such that OML in the whole ocean is under the weak surface wind forcing (Fig. 3a). Therefore, the decrease of OML depth ($h_w < 0$) leads to the augmentation of SST perturbation ($\partial T_s/\partial t > 0$) and in turn to a production of the atmospheric convection to the west of the initial convective region (Fig. 3a) due to additional moisture convergence and surface evaporation associated with the augmentation of SST perturbation.

(ii) *Strong mean easterlies and weak initial perturbation.* In this case, the total surface winds, which are the summation of the mean easterlies and the surface wind perturbation associated with the initial positive SST fluctuation, are strong such that OML in the whole ocean is under strong surface wind forcing (Fig. 3b). Therefore, the increase of OML depth ($h_w > 0$) leads to the augmentation of SST perturbation ($\partial T_s/\partial t > 0$) and in turn to a production of the atmospheric convection to the east of the initial convective region (Fig. 3b) due to additional moisture convergence and surface evaporation associated with the augmentation of SST perturbation.

(iii) *Strong initial perturbation.* If the zonal circulation associated with the initial convection is strong enough in the east of the warm water, OML is under strong surface wind forcing; and in the west of the warm water, OML is under weak surface wind forcing. In the east of the warm water (under strong surface wind forcing), the increase of OML depth ($h_w > 0$) leads to the augmentation of SST perturbation ($\partial T_s/\partial t > 0$) and in turn to a production of the atmospheric convection to the east of the initial convective region (Fig. 3c). In the west of the warm water (under weak surface wind forcing), the decrease of OML depth ($h_w < 0$) leads to the augmentation of SST perturbation ($\partial T_s/\partial t > 0$) and in turn to a production of the atmospheric

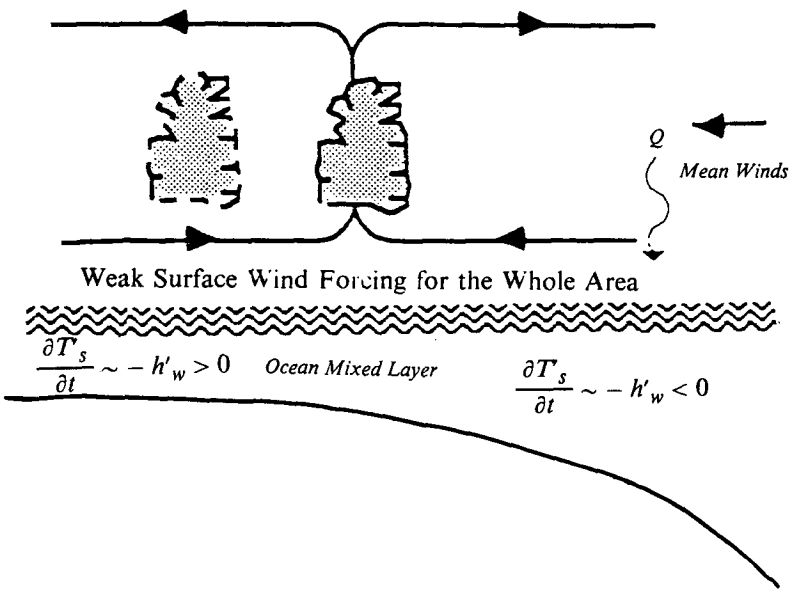

FIG. 3. Atmospheric convection generated by the air–ocean feedback mechanism under (a) weak surface wind forcing, (b) strong surface wind forcing, and (c) strong initial perturbation.

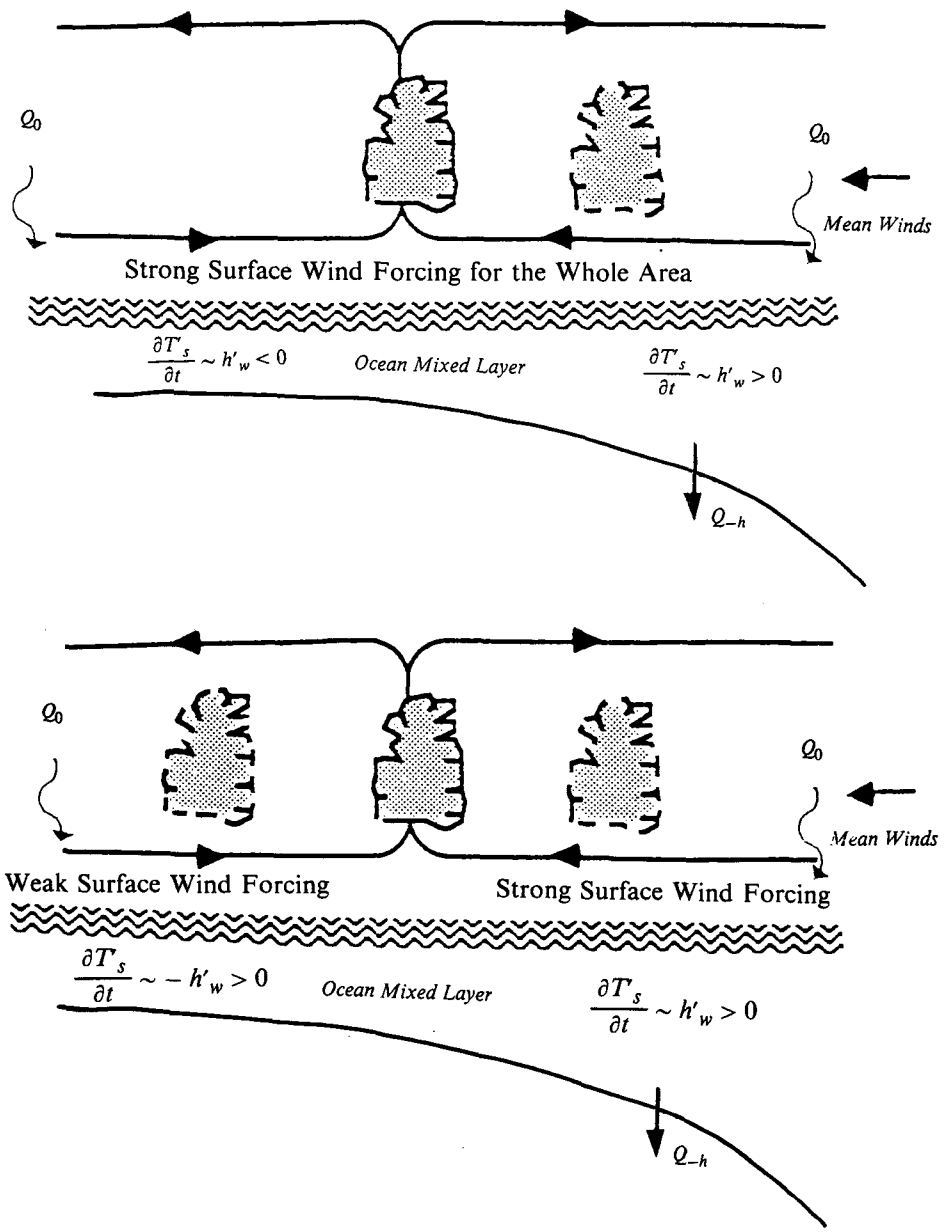

FIG. 3. (*Continued*)

convection to the west of the initial convective region (Fig. 3c). Therefore, when the initial perturbation is strong, the atmospheric convection will be generated in both east and west sides of the initial convective area.

The unstable modes generated by this air–ocean feedback mechanism are called AOSHE modes, which are largely determined by the ocean surface condition. When the ocean surface is under weak surface wind forcing this mode propagates *westward,* however, when the ocean surface is under strong surface wind forcing this mode propagates *eastward.* Such a distinction will largely impact upon our understanding about the unstable equatorial low-frequency modes.

5. Nondimensional system

The equations are nondimensionalized following E87:

$$x^* = ax, \quad y^* = a^{1/4}A^{1/4}\beta^{-1/2}y, \quad z^* = H_m z,$$
$$h_w^* = \langle h_w \rangle h_w, \quad t^* = a^{1/2}A^{-1/2}t,$$
$$u^* = a^{1/2}A^{1/2}u, \quad v^* = a^{-1/4}A^{3/4}\beta^{-1/2}v,$$

$$w^* = H_m A^{1/2} a^{-1/2} w,$$

$$\delta\phi^* = \bar{\epsilon} c_{pa} T_b \Delta\phi = aA\phi, \quad \delta \ln\theta^* = \Delta T_{eb}/\hat{\Gamma},$$

$$\delta \ln\theta^*_{eb} = \Delta T_{eb}, \quad \delta \ln\theta^*_{em} = \Delta T_{em},$$

$$\delta \ln\theta^*_{es} \approx \frac{T^*_s}{\langle T_s \rangle} = \Delta T_{es}, \tag{23}$$

where the asterisks denote the dimensional values. Definitions and typical values of the constants are

$$A = \bar{\epsilon} c_{pa} T_b C_\theta H^{-1} \ln(\langle\theta_{es}\rangle/\langle\theta_{eb}\rangle)$$

$$\approx 1.26 \times 10^{-4} \text{ m s}^{-2},$$

$$\Delta = aH^{-1}C_\theta \ln(\langle\theta_{es}\rangle/\langle\bar{\theta}_{eb}\rangle) \approx 4.4 \times 10^{-2},$$

$$\hat{\Gamma} = \Gamma_d/\Gamma_m \approx 1.7.$$

Also note that

$$A = (\bar{\epsilon} c_{pa} T_b/a)\Delta.$$

Everything in (23) is the same as in YE91 except that the SST perturbation is included.

The physical values of the model constants are listed in Tables 1 and 2. From these values, the characteristic time and velocity scales are

$$a^{1/2}A^{-1/2} = 2.25 \times 10^5 \text{ s} = 2.6 \text{ d},$$

$$a^{1/2}A^{1/2} = 28.4 \text{ m s}^{-1}. \tag{24}$$

a. Atmospheric component

From the foregoing, a nondimensional set of equations for the atmospheric part is given by

$$(D + 2F)u_b = ik(T_{eb} - \bar{\phi}) + yv_b, \tag{25a}$$

$$(D + F)v_b = P\left[\frac{d(T_{eb} - \bar{\phi})}{dy} - yu_b\right], \tag{25b}$$

TABLE 1. Standard values for atmospheric model constants (after YE91).

$a = 6.38 \times 10^6$ m	radius of the earth
$\beta = 2.3 \times 10^{-8}$ s^{-1} km^{-1}	meridional gradient of the Coriolis parameter
$g = 9.8$ m s^{-2}	gravitational acceleration
$N^2 = 10^{-4}$ s^{-2}	Brunt–Väisälä frequency
$H = 8$ km	thickness of the troposphere
$H_m = 5$ km	level of minimum θ_e in the troposphere
$h = 500$ m	thickness of the subcloud layer
$C_D = 1 \times 10^{-3}$	bulk coefficient of the momentum exchange rate
$C_\theta = 1.2 \times 10^{-3}$	bulk coefficient of the entropy exchange
$\bar{\epsilon} = 0.1$	thermodynamic efficiency
$\ln(\bar{\theta}_{es}/\bar{\theta}_{eb}) = 0.035$	thermodynamic disequilibrium
$\lvert U\rvert = 2$ m s^{-1}	magnitude of mean zonal wind
$C_{pa} = 1000$ J kg^{-1} K^{-1}	air specific heat at constant pressure
$\tau_{rad} = 50$ d	radiative time scale
$\rho_{a0} = 1.29$ Kg m^{-3}	characteristic air density

TABLE 2. Standard values for oceanic model constants.

$\rho_{w0} = 1.034 \times 10^3$ Kg m^{-3}	
$c_{pw} = 4186$ J kg^{-1} K^{-1}	
$C_1 = 1.0$	
$C_2 = 0.2$	
$\langle h_w \rangle = 50$ m	
$\langle w_{-\delta E} \rangle = 1$ m day^{-1}	
$\delta T = 3$ K	
$\langle T_s \rangle = 300$ K	
$\langle Q_0 \rangle = 80$ W m^{-2}	

$$iku_b + \frac{dv_b}{dy} + (1 - \sigma)w_d + \sigma w_c = 0, \tag{25c}$$

$$(D + \alpha_R)T_{eb} = -\hat{\Gamma}\lambda(1 - \sigma)w_d, \tag{25d}$$

$$(\delta D + \alpha_e + \alpha_D)T_{eb} = \text{sgn}(U)u_b + \alpha_e T_{es} + \lambda[-(1 - \epsilon_p)\sigma w_c + \epsilon_p(1 - \sigma)w_d] + \alpha_D T_{em}, \tag{25e}$$

$$(D + \alpha_D)T_{em} = \lambda(1 - \epsilon_p)\sigma w_c + [\alpha_D - (\alpha_R/\hat{\Gamma})]T_{eb} - \epsilon_p\lambda(1 - \sigma)w_d, \tag{25f}$$

where the terms T_{es}, $\bar{\phi}$ are used for the coupling with OML and the stratosphere, respectively. The effect of the stratosphere, which has been discussed in YE91, is ignored in this research, that is, $\bar{\phi} = 0$ will be taken, corresponding to a rigid lid at the tropopause. Here, as in YE91, the model solutions are assumed to have the form

$$\exp(ikx + \omega t),$$

and also

$$D \equiv \omega + ikU, \quad P \equiv \beta A^{-1/2} a^{3/2}$$

are introduced. Note that U in the definition of D is nondimensionalized by the factor $A^{1/2}a^{1/2}$. The parameter P is very important in determining the dynamical feature of the atmosphere. If P is large, the zonal wind perturbation is in geostrophic balance; if P is small, the meridional wind becomes negligible, and the Kelvin-like mode dominates the atmosphere.

The nondimensional parameters that appear in (25a–f) are defined with approximate magnitudes by (see YE91):

$$F \equiv C_D|U^*|a^{1/2}A^{-1/2}h^{-1} \sim 0.9,$$

$$\delta \equiv h/H \sim 0.0625,$$

$$\lambda \equiv N^2 H_m/g\delta \sim 1,$$

$$\alpha_R \equiv a^{1/2}A^{-1/2}/\tau_{rad} \sim 0.05,$$

$$\alpha_e \equiv C_\theta|U^*|a^{1/2}A^{-1/2}/H \sim 0.07,$$

$$\alpha_D \equiv \epsilon_p \frac{a^{1/2}A^{-1/2}C_\theta|U^*|}{H^2N^2} g \ln\left(\frac{\bar{\theta}_{es}}{\bar{\theta}_{eb}}\right) \sim \frac{0.03}{\epsilon_p}. \tag{26}$$

These parameters are kept the same as in YE91 for easy comparison between the WISHE and AOSHE

models. Detailed discussion on the physical significance of these parameters can be found in YE91.

b. Oceanic component with a weak surface wind forcing

Nondimensionalization of the perturbation heat equation under weak surface wind forcing (17) leads to

$$(D + \alpha_s^{(w)} - ikU)T_{es} = -\alpha_u^{(w)} \operatorname{sgn}(U) u_b, \quad (27)$$

where

$$\alpha_s^{(w)} \equiv \frac{a^{1/2}A^{-1/2}}{\tau_T} \approx 0.005 \quad (28a)$$

$$\alpha_u^{(w)} \equiv \frac{[3\langle Q_0\rangle + \rho_{a0}c_{pa}C_\theta|U^*|(\langle\theta_{es}\rangle - \langle\theta_{eb}\rangle)]a}{\rho_{w0}c_{pw}\langle h_w\rangle|U^*|\langle T_s\rangle\Delta} \approx 0.268 \quad (28b)$$

are the nondimensional thermal dissipation coefficient and the air–ocean coupling coefficient, respectively. The superscript (w) indicates the weak surface wind forcing. The numerical values are obtained by use of the model constants listed in Tables 1 and 2.

Elimination of u_b and T_{eb} from the atmospheric momentum equations (25a), (25b), and the SST equation (27) leads to

$$G^{(w)}T_{es} = -\left[ika_3\frac{dv_b}{dy} + a_1 y v_b\right]\alpha_u^{(w)} \operatorname{sgn}(U), \quad (29)$$

which shows the oceanic heat redistribution caused by weak surface winds. Here $G^{(w)}$, a_1, and a_3 are fourth-order, second-order, and first-order polynomials of D,

$$G^{(w)} \equiv (D + \alpha_s^{(w)} - ikU)P_3(D) + ik\alpha_u^{(w)}\alpha_e(D + \alpha_D)\operatorname{sgn}(U),$$

$$a_1 = (D + \alpha_D)(\delta D + \alpha_D + \alpha_e) + \frac{\alpha_D\alpha_R}{\hat{\Gamma}} - \alpha_D^2 + \frac{D(D + \alpha_R)}{\hat{\Gamma}},$$

$$a_3 = D\lambda(1 - \epsilon_p), \quad (30)$$

where $P_3(D)$ is a third-order polynomial:

$$P_3(D) \equiv B_1D^3 + B_2D^2 + B_3D + B_4, \quad (31a)$$

where

$$B_1 \equiv \delta + \hat{\Gamma}^{-1},$$

$$B_2 \equiv B_1\alpha_D + \alpha_e + \alpha_D + 2FB_1 + \frac{\alpha_R - \alpha_D}{\hat{\Gamma}},$$

$$B_3 \equiv \alpha_D(\alpha_e + \alpha_R\hat{\Gamma}^{-1}) + 2F(B_2 - 2FB_1) + ik + (1 - \epsilon_p)\lambda k^2,$$

$$B_4 \equiv \alpha_D[2F(\alpha_e + \alpha_R\hat{\Gamma}^{-1}) + ik]. \quad (31b)$$

The roots of the third-order algebraic equation

$$P_3(D) = 0$$

are the eigenvalues of the WISHE model (YE91).

c. Oceanic component with a strong surface wind forcing

Nondimensionalization of a set of OML dynamical and thermodynamical equations for a strong surface wind forcing (21) and (22) leads to

$$[D + \alpha_s^{(s)} - ikU]T_{es} = -\alpha_u^{(s)} \operatorname{sgn}(U)u_b + \alpha_h h_w \quad (32)$$

$$(D + \mu - ikU)h_w = \frac{\langle T_s\rangle}{\delta T}\alpha_u^{(s)} \operatorname{sgn}(U)u_b + \alpha_T T_{es}, \quad (33)$$

where

$$\alpha_s^{(s)} \equiv \frac{(1 + C_2)a^{1/2}A^{-1/2}}{2\tau_T} \approx 0.003, \quad (34a)$$

which is the thermal dissipation coefficient, and

$$\alpha_u^{(s)} \equiv \frac{a}{|U^*|\langle T_s\rangle\Delta}\left[3\left(\frac{C_2\langle Q_0\rangle}{\rho_{w0}c_{pw}\langle h_w\rangle} + \frac{\langle w_{-h}\rangle}{\langle h_w\rangle}\delta T\right) + \frac{(1 + C_2)\rho_{a0}c_{pa}C_\theta|U|(\langle\theta_{es}\rangle - \langle\theta_{eb}\rangle)}{\rho_{w0}c_{pw}\langle h_w\rangle}\right] \approx 0.18 \quad (34b)$$

which is the air–ocean coupling coefficient. The superscript (s) indicates the strong surface wind forcing. The other nondimensional parameters for OML in (32) and (33) are defined by

$$\alpha_h \equiv \frac{a^{1/2}A^{-1/2}}{\Delta\langle T_s\rangle}\left[\frac{(C_2 - 1)\langle Q_0\rangle}{\rho_{w0}c_{pw}\langle h_w\rangle} + \frac{2\langle w_{-h}\rangle}{\langle h_w\rangle}\delta T\right] \approx 0.0059,$$

$$\alpha_T \equiv a^{1/2}A^{-1/2}\left[\frac{C_2\Delta\langle T_s\rangle\tau_T^{-1}}{2\delta T} - \frac{\langle w_{-h}\rangle\Delta\langle T_s\rangle}{\langle h_w\rangle\delta T}\right] \approx -0.0343,$$

$$\mu \equiv a^{1/2}A^{-1/2}\left(\frac{C_2\langle Q_0\rangle}{\rho_{w0}c_{pw}\langle h_w\rangle\delta T} + \frac{\langle w_{-h}\rangle}{\langle h_w\rangle}\right) \approx 0.018. \quad (34c)$$

These parameters are evaluated by a set of physical values for the model constants representing the general equatorial Pacific Ocean conditions shown in Table 2, where $\langle w_{-\delta_E}\rangle$ is designated the vertical velocity at the base of the Ekman layer. From Wyrtki's (1981) estimation, the mean upwelling velocity at the base of the Ekman layer ($z = -\delta_E$) is nearly 1 m day^{-1}. Theoretically, the Ekman depth at the equator is infinity. If $\delta_E \approx 200$ m is thought to be a reasonable estimation of

Ekman layer thickness, the mean vertical velocity at the OML mean depth can be roughly estimated by

$$\langle w_{-h}\rangle \approx \frac{\langle h_w\rangle}{\langle \delta_E\rangle} w_{-h_E} \approx 0.25 \text{ m day}^{-1}.$$

Elimination of h_w from (32) and (33) leads to

$$(D + \alpha_s^{(s)} - ikU)(D + \mu - ikU)T_{es} = -\alpha_u^{(s)} \operatorname{sgn}(U)\left(D + \mu - \frac{\langle T_s\rangle}{\delta T}\alpha_h - ikU\right)u_b + \alpha_h\alpha_T T_{es}. \quad (35)$$

The last term on the right-hand side of (35), $\alpha_h\alpha_T T_{es}$, is very small ($\alpha_h\alpha_T \sim 10^{-5}$) and will be neglected.

Elimination of u_b and T_{eb} from the atmospheric momentum equations (25a), (25b), and the SST equation (35) leads to

$$G^{(s)}T_{es} = -\left[ika_3\frac{dv_b}{dy} + a_1 y v_b\right]\alpha_u^{(s)} \operatorname{sgn}(U), \quad (36)$$

which shows the oceanic heat redistribution by the surface winds. Here $G^{(s)}$ is defined by

$$\left(D + \mu - \frac{\langle T_s\rangle}{\delta T}\alpha_h - ikU\right)G^{(s)} \equiv (D + \alpha_s^{(s)} - ikU)(D + \mu - ikU)P_3(D) + ik\alpha_u^{(s)}\alpha_e \operatorname{sgn}(U)(D + \alpha_D) \times \left(D + \mu - \frac{\langle T_s\rangle}{\delta T}\alpha_h - ikU\right). \quad (37)$$

d. Eigenvalue problem

Elimination of T_{es} from the atmospheric equation (25) and the SST equation (29) for the weak surface forcing or SST equation (36) for strong surface wind forcing becomes a single equation for v_b:

$$\frac{d^2v_b}{dy^2} + \mathscr{H}_1 y\frac{dv_b}{dy} + \mathscr{H}_2(1 - \mathscr{H}_3 y^2)v_b = 0, \quad (38)$$

where

$$\mathscr{H}_1 = \frac{G(a_2 - ika_3) - a_1a_4(D + 2F)\alpha_u \operatorname{sgn}(U) - k^2a_3a_4\alpha_u \operatorname{sgn}(U)}{(D + 2F)a_3(D + \alpha_s - ikU)P_3(D)}$$

$$\mathscr{H}_2 = \frac{G[a_2 - P^{-1}P_3(D)(D + F)]}{(D + 2F)a_3(D + \alpha_s - ikU)P_3(D)}$$

$$\mathscr{H}_3 = \frac{a_1(D + \alpha_s - ikU)P_3(D)}{G[a_2 - P^{-1}P_3(D)(D + F)]}, \quad (39)$$

where (G, α_u, α_s) is taken as $(G^{(w)}, \alpha_u^{(w)}, \alpha_s^{(w)})$ for weak surface wind forcing and as $(G^{(s)}, \alpha_u^{(s)}, \alpha_s^{(s)})$ for strong surface wind forcing; a_2, a_4 are linear functions of D:

$$a_2 = [D\lambda(1 - \epsilon_p)ik + (D + \alpha_D)\operatorname{sgn}(U)],$$
$$a_4 = \alpha_e(D + \alpha_0).$$

Let

$$\eta = i\left(\frac{\mathscr{H}_1}{2\mathscr{J}}\right)^{1/2} y, \quad v_b = \hat{v}_b(\eta)e^{(\mathscr{J}\eta^2/2)}, \quad (40a)$$

where

$$\mathscr{J} = \frac{1}{(1 + 4\mathscr{H}_2\mathscr{H}_3/\mathscr{H}_1^2)^{1/2}}. \quad (40b)$$

The subcloud-layer meridional wind equation (38) becomes

$$\frac{d^2\hat{v}_b}{d\eta^2} + \left(\mathscr{J} - \frac{2\mathscr{J}\mathscr{H}_2}{\mathscr{H}_1} - \eta^2\right)\hat{v}_b = 0, \quad (41)$$

which has analytical solutions

$$\hat{v}_b = e^{-(\eta^2/2)}H_n(\eta), \quad n = 0, 1, 2, \cdots \quad (42)$$

for

$$\mathscr{J} - 2\mathscr{J}\frac{\mathscr{H}_2}{\mathscr{H}_1} = 2n + 1, \quad (43)$$

which is the dispersion relation. Here $H_n(\eta)$ is the Hermite polynomial with integer order n. The meridional wind in the subcloud layer becomes

$$v_b = \hat{v}_b(\eta)e^{(\mathscr{J}\eta^2)/2} = e^{[(1-\mathscr{J})\eta^2]/2}H_n(\eta) = e^{-\{[(1-\mathscr{J})\mathscr{H}_1]/4\mathscr{J}\}y^2}H_n\left(i\left(\frac{\mathscr{H}_1}{2\mathscr{J}}\right)^{1/2}y\right).$$

By the use of the dispersion relation (43) we get

$$v_b = \exp\left[-\frac{(n\mathscr{H}_1 + \mathscr{H}_2)}{2(2n + 1)\mathscr{H}_1}y^2\right]H_n\left(i\left(\frac{\mathscr{H}_1}{2\mathscr{J}}\right)^{1/2}y\right). \quad (44)$$

Thus, in order to get a well-behaved solution,

$$\operatorname{Re}\left(\frac{\mathscr{H}_2}{\mathscr{H}_1}\right) \geq 0, \quad \text{for} \quad n = 0$$

$$\operatorname{Re}\left(n + \frac{\mathscr{H}_2}{\mathscr{H}_1}\right) > 0, \quad \text{for} \quad n = 1, 2, \cdots. \quad (45)$$

The validity of equality for $n = 0$ is due to the boundness of H_0.

The primary purpose now is to discuss new insight on low-frequency modes brought on by the existence of the two-way correlation between time rate of change of SST and OML depth, rather than to do a mathematical exercise. Therefore, only the zero-order mode ($n = 0$) is considered. Substitution of (40b) into (43) for $n = 0$ leads to

$$\mathscr{H}_2 = \mathscr{H}_1 + \mathscr{H}_3, \quad (46)$$

which is

$$G^2P_3^2(D)(D+F)^2 - PP_3(D)(D+F) \times G[ika_3 + a_1a_4(D+2F)\alpha_u \operatorname{sgn}(U) + k^2a_3a_4\alpha_u \operatorname{sgn}(U) + a_2G] + P^2\{Ga_2[ika_3 + a_1a_4(D+2F)\alpha_u \operatorname{sgn}(U) + k^2a_3a_4\alpha_u \operatorname{sgn}(U)] - (D+2F)a_1a_3 \times (D+\alpha_s - ikU)P_3^2(D)\} = 0. \quad (47)$$

For a small value of P, the dispersion relation (47) is simplified as

$$G^2P_3^2(D)(D+F)^2 \approx 0, \quad (48)$$

which can be separated into three algebraic equations:

$$P_3(D) = 0, \quad G(D) = 0, \quad (D+F) = 0,$$

where $P_3(D) = 0$ is the dispersion relation for the WISHE model; $D + F = 0$, represents the damping modes with decay rate $-F$ (not of interest here); and

$$G(D) = 0, \quad (49)$$

which is the dispersion relation for new modes appearing only in the AOSHE model. By the use of (39), this solution (49) leads to

$$\mathscr{H}_2 = 0,$$

which indicates that the eigenvalue solutions are well-behaved solutions [see Eq. (45)]. The AOSHE solution for large values of P and higher orders ($n = 1, 2, \cdots$) will be discussed in future studies.

6. AOSHE mode under weak surface wind forcing (AOSHE W-Mode)

For a weak surface wind forcing, $G = G^{(w)}$, and the dispersion relation (49) becomes

$$(D + \alpha_s - ikU)P_3(D) + ik\gamma^{(w)} \operatorname{sgn}(U)(D + \alpha_D) = 0, \quad (50)$$

where

$$\gamma^{(w)} \equiv \alpha_u^{(w)}\alpha_e \approx 0.02, \quad (51)$$

which comes from the air–ocean coupling. The value of $\gamma^{(w)}$ is estimated by (26) and (28b). If there is no air–sea feedback, $\gamma^{(w)} = 0$, the dispersion relation (50) is reduced to

$$P_3(D) = 0.$$

Generally speaking, the fourth-order algebraic equation (50) has four roots. For a given set of nondimensional parameters, only two of the four roots of (50) have positive real parts representing unstable modes. The remaining two or more roots all have negative real parts representing damped modes, which are not of interest here and are therefore neglected. Among the two unstable modes, one is high frequency (30–60 day), and the other is low frequency (interannual). The high-frequency mode is the modified WISHE mode. The low-frequency mode is called the AOSHE W-Mode, that is, the AOSHE mode under weak surface wind forcing. The nondimensional parameters in the dispersion relation (50), $\gamma^{(w)}$, $\alpha_s^{(w)}$, λ, F, and ϵ_p, will be varied in the present study in order to investigate the sensitivity of the model. The physical significance of all the parameters except $\gamma^{(w)}$ and $\alpha_s^{(w)}$ are discussed in YE91. Here $\gamma^{(w)}$ and $\alpha_s^{(w)}$ denote the strength of the air–ocean coupling and OML thermal dissipation.

a. Sensitivity to air–ocean coupling parameter $\gamma^{(w)}$

The dispersion relation (50) is solved for the eigenvalue D for $\alpha_s^{(w)} = 0.005$, $F = 0.1$, $\epsilon_p = 0.8$, $\lambda = 1$, and for five different values of $\gamma^{(w)}$: 0.01, 0.02, 0.03, 0.04, 0.05. For $\gamma^{(w)} = 0$, referring to the air–ocean decoupled case (AOSHE reduced to WISHE), there is no AOSHE W-Mode. For $\gamma^{(w)} \neq 0$, the AOSHE W-Mode is generated. Figure 4 demonstrates the sensitive dependence of $\gamma^{(w)}$ of the AOSHE W-Mode. For a given wavenumber k, the growth rate increases monotonically with $\gamma^{(w)}$.

The AOSHE W-Mode has the following features.

(i) *Largest-scale mode selection.* The growth rate D_r has its maximum at the lowest wavenumber, indicating that the largest scale grows most rapidly. The growth rate decreases monotonically as k increases. For a given $\gamma^{(w)}$, there exists a critical wavenumber k_c. The larger scale ($k < k_c$) AOSHE W-Mode is a growing mode; however, the smaller scale ($k > k_c$) AOSHE W-Mode is a damping mode. This criterion k_c increases monotonically with $\gamma^{(w)}$: $k_c \approx 5$ for $\gamma^{(w)} = 0.01$ to $k_c \approx 15$ for $\gamma^{(w)} = 0.05$. As $k \to \infty$, the growth rate tends to a negative value for all $\gamma^{(w)}$, which shows that the smallest-scale disturbance damps fastest (a distinct feature from the WISHE mode).

(ii) *Slow growth.* The maximum growth rate of the AOSHE W-Mode (on the order of 2.4 yr^{-1} for $\gamma^{(w)} = 0.02$) is nearly 1.6% of that of the WISHE mode. The growth rate increases with the augmentation of $\gamma^{(w)}$, which depends on $\langle Q_0 \rangle$, C_θ, A, $\langle h_w \rangle$, $\langle T_s \rangle$, H, and Δ. The weaker the surface wind forcing, the shallower the OML, and in turn the larger the value of $\gamma^{(w)}$; and hence, the faster growing of the AOSHE W-Mode.

(iii) *Low frequency.* The AOSHE W-Mode is a low-frequency mode. The period, $\text{Pe} = 2\pi/|kc|$, of the unstable mode is nearly 2–10 years (Fig. 4b). Such a frequency is on the same order of the ENSO frequency.

(iv) *Slow westward propagation.* The AOSHE W-Mode slowly propagates westward. The phase speed in all cases is smaller than 0.3 m s^{-1} (Fig. 4c). Similar to the growth rate, the phase speed also has its maximum at the lowest wavenumber. The phase speed tends to zero as the wavenumber k tends to infinity. The phase

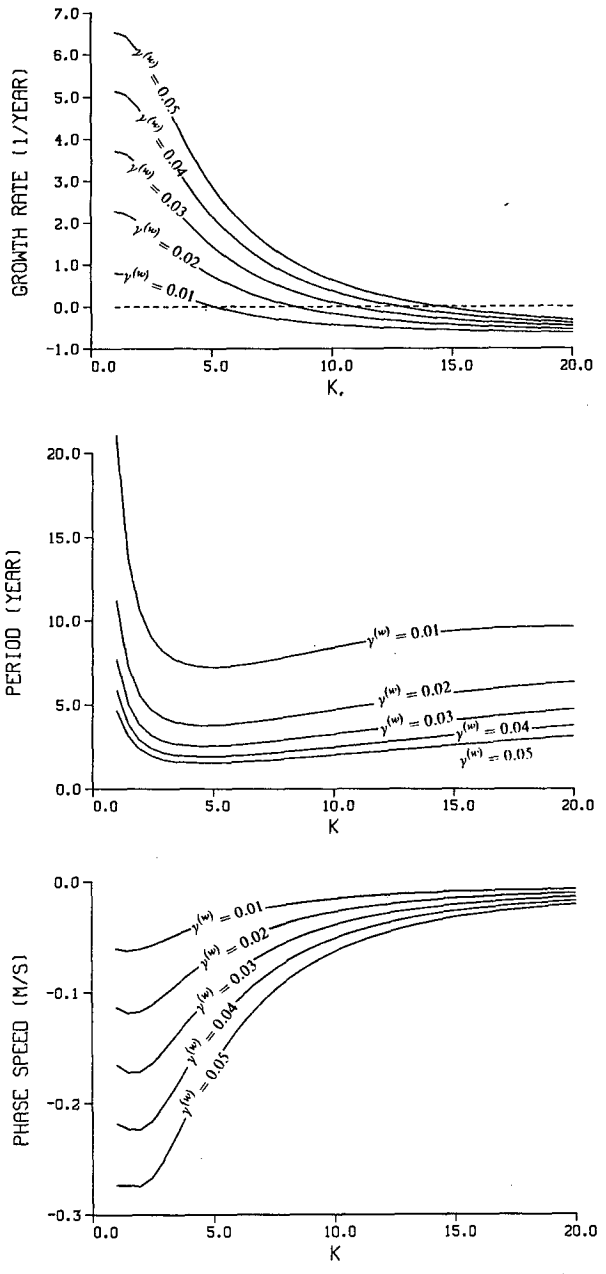

FIG. 4. The dependence of (a) growth rate, (b) period, and (c) phase velocity of the AOSHE W-Mode in the mean easterlies ($U^* = -2$ m s^{-1}, on longitudinal wavenumber k for various values of the air–ocean coupling parameter $\gamma^{(w)}$. The other important parameters are $\alpha_s^{(w)} = 0.005$, $F = 0.1$, $\epsilon_p = 0.8$, and $\lambda = 1$.

speed increases with the augmentation of $\gamma^{(w)}$. The phase speed for unstable AOSHE W-Mode (10–30 cm s^{-1}) shows a quite good agreement with the observed westward phase speed (20 cm s^{-1}) of the equatorial Pacific 14°C isotherm-depth perturbation (Meyers 1979) and with the observed westward phase speed (30–50 cm s^{-1}) of the surface wind and ocean signals (Michum and Lukas 1987).

The solutions show that there is almost no effect of air–ocean coupling on the high-frequency mode (30–60 day), which means that only the WISHE mechanism is responsible for the generation of the intraseasonal variation.

b. *Sensitivity to* $\alpha_s^{(w)}$

The dispersion relation (50) is solved for the eigenvalue D for $\gamma^{(w)} = 0.02$, $F = 0.1$, $\epsilon_p = 0.8$, $\lambda = 1$, and for five different values of $\alpha_s^{(w)}$: 0, 0.002, 0.005, 0.01, 0.02. Figure 5 indicates the sensitivity of the AOSHE W-Mode growth rate on the thermal dissipation coefficient $\alpha_s^{(w)}$.

(i) For a given wavenumber k, the growth rate decreases monotonically with $\alpha_s^{(w)}$. For $\alpha_s^{(w)} = 0$ (no thermal dissipation in OML), the growth rate is always positive and tends to zero as $k \mapsto \infty$.

(ii) When $\alpha_s^{(w)} > 0$, a wavenumber criterion k_c exists such that the larger scale ($k < k_c$) AOSHE W-Mode is growing, and the smaller scale ($k > k_c$) AOSHE W-Mode is damping. This criterion k_c decreases monotonically with the increasing $\alpha_s^{(w)}$ from $k_c \approx 15$ for $\alpha_s^{(w)} = 0.002$, to $k_c \approx 2$ for $\alpha_s^{(w)} = 0.02$.

Furthermore, a very slight effect of $\alpha_s^{(w)}$ on the AOSHE W-Mode phase speed was found. In the largest scale $k < 3$, the augmentation of the thermal dissipation $\alpha_s^{(w)}$ increases the phase speed by a few percent. For $k > 3$, there is no effect of $\alpha_s^{(w)}$ on the AOSHE W-Mode phase speed.

c. *Sensitivity to the mean easterlies* U^*

The annual mean easterlies in the central and eastern Pacific are about 5 m s^{-1}, while in the western Pacific they are about 2 m s^{-1}. In order to address the model sensitivity with respect to U^*, we solve the dispersion

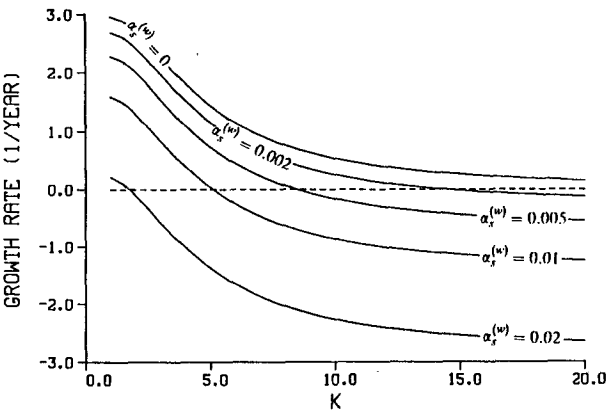

FIG. 5. The dependence of the growth rate of the AOSHE W-Mode in the mean easterlies ($U^* = -2$ m s^{-1}) on longitudinal wavenumber k for various values of the OML thermal dissipation $\alpha_s^{(w)}$. The other important parameters are $\gamma_w = 0.02$, $F = 0.1$, $\epsilon_p = 0.8$, and $\lambda = 1.0$.

relation (50) for $F = 0.1$, $\gamma^{(w)} = 0.02$, $\alpha_s^{(w)} = 0.005$, $\epsilon_p = 0.8$, $\lambda = 1$, and for five different values of U^*: -1 m s^{-1}, -2 m s^{-1}, -3 m s^{-1}, -4 m s^{-1}, and -5 m s^{-1}.

Figure 6 shows the dependence of growth rate and phase speed of the AOSHE W-Mode on k for different values of U^*. It is noticed that the growth rate (Fig. 6a) for the whole wavenumber domain and the phase speed (Fig. 6b) for $k > 3$ are insensitive to the mean wind; however, for $k < 3$, the westward phase speed increases with the increasing U^*. Not much variation in both growth rate and phase speed for different values of U^* indicates that the AOSHE mechanism is valid for the whole ocean basin (western, central, and eastern) when OML is in the shallowing regime.

7. AOSHE mode under strong surface wind forcing (AOSHE S-Mode)

For a strong surface wind forcing, $G = G^{(s)}$, and the dispersion relation (49) becomes

$$(D + \alpha_s^{(s)} - ikU)(D + \mu - ikU)P_3(D) = -ik\gamma^{(s)}\,\mathrm{sgn}(U)(D + \alpha_D)(D + \mu - \gamma_e - ikU), \quad (52)$$

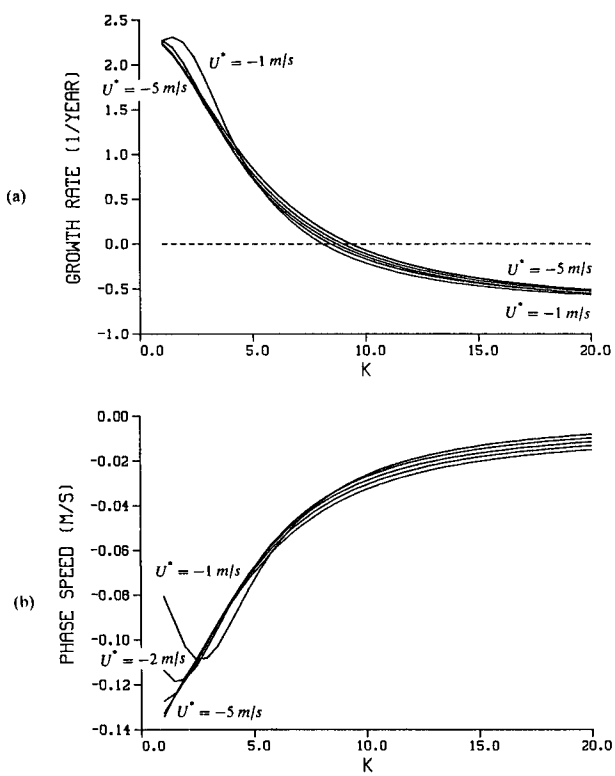

FIG. 6. The dependence of the (a) growth rate and (b) phase velocity of the AOSHE W-Mode on longitudinal wavenumber k for various values of the mean easterlies U^*. The other important parameters are $\gamma^{(w)} = 0.02$, $\alpha_s^{(w)} = 0.005$, $F = 0.1$, $\lambda = 1$, and $\epsilon_p = 0.8$.

where

$$\gamma^{(s)} \equiv \alpha_u^{(s)}\alpha_e \sim 0.01, \quad \gamma_e \equiv \alpha_h \frac{\langle T_s \rangle}{\delta T} \sim 0.1, \quad (53)$$

which are two important parameters representing the ocean–atmosphere surface coupling and the OML entrainment process. Here, the values of $\gamma^{(s)}$ and γ_e are estimated by the use of (26), (34b), (34c), and Table 2. It is noticed that if there is no air–sea feedback, $\gamma^{(s)} = 0$, the dispersion relation (52) is reduced to $P_3(D) = 0$, that is, the AOSHE model reduces to the WISHE model. The physical significance of γ_e denotes the strength of the entrainment mixing. The larger the value of γ_e, the stronger the entrainment process in the OML.

Generally speaking, the fifth-order algebraic equation (52) has five roots. For a given set of nondimensional parameters, at most two of the five roots of (52) have positive real parts representing unstable modes. Among them, one is similar to the WISHE solution (i.e., high-frequency mode), and the other is a new solution only appearing in the AOSHE model and representing a low-frequency unstable mode called AOSHE S-Mode. The other three roots all have negative real parts representing dampening modes, which are not of interest here and are therefore neglected. The five nondimensional parameters in the dispersion relation (52), $\gamma^{(s)}$, γ_e, $\alpha_s^{(s)}$, F, ϵ_p, will be varied in the present study in order to investigate the sensitivity of the model.

a. Sensitivity to air–ocean coupling parameter $\gamma^{(s)}$

The dispersion relation (52) is solved for the eigenvalue D for $\gamma_e = 0.1$, $\alpha_s^{(s)} = 0.006$, $F = 0.1$, $\epsilon_p = 0.8$, $\lambda = 1$, and for five different values of $\gamma^{(s)}$: 0.005, 0.01, 0.02, 0.03, and 0.04.

The growth rate and phase speed remain unchanged for all $\gamma^{(s)}$ for the high-frequency (30–60 day) mode. This indicates that the WISHE mechanism is responsible for the generation of the high-frequency (30–60 day) mode. The air–sea coupling is not important for such a mode.

Figure 7 demonstrates that the sensitive dependence of $\gamma^{(s)}$ actually leads to the generation of the low-frequency (interannual) AOSHE S-Mode. For $\gamma^{(s)} = 0$, referring to the air–ocean decoupled case, the AOSHE mode does not appear; for $\gamma^{(s)} \neq 0$, the AOSHE S-Mode does appear.

The AOSHE S-Mode has the following features (Fig. 7):

(i) *Length-scale mode selection.* The growth rate D_r has its maximum in the wavenumber domain. The maximum growth rate shifts toward the lower wavenumber side as $\gamma^{(s)}$ increases, that is, the wavenumber with maximum growth rate, $k_{\max}$, changes from $k_{\max} \approx 5$ for $\gamma^{(s)} = 0.005$, to $k_{\max} \approx 4$ for $\gamma^{(s)} = 0.03$.

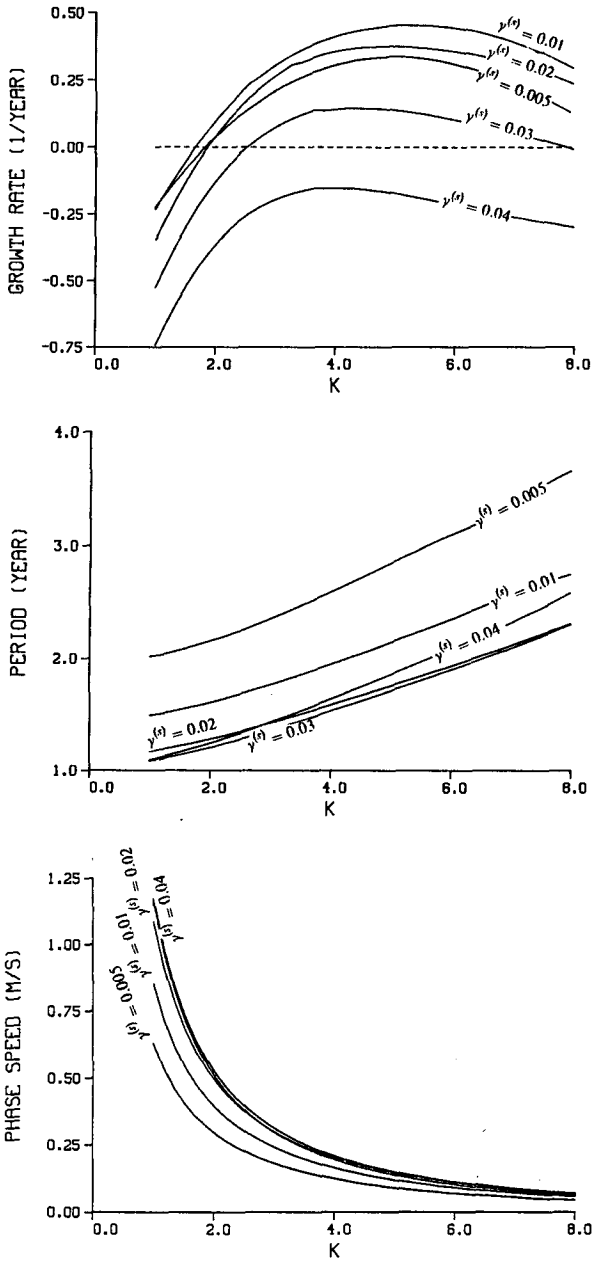

FIG. 7. Dependence of the low-frequency AOSHE S-Mode on the coupling parameter $\gamma^{(s)}$: (a) growth rate, (b) period, and (c) phase speed. The other important parameters are $\gamma_e = 0.1$, $\alpha_s^{(s)} = 0.006$, $F = 0.1$, $\epsilon_p = 0.8$, and $\lambda = 1$.

(ii) *Slow growth.* The maximum growth rate of the AOSHE S-Mode is 0.46 yr^{-1} for $\gamma^{(s)} = 0.01$, which is much smaller than the AOSHE W-Mode.

(iii) *Λ-type effect on growth rate.* It is interesting to see the Λ-type effect of the air–ocean coupling coefficient $\gamma^{(s)}$ on the growth rate of the AOSHE S-Mode: the growth rate generally increases with increasing $\gamma^{(s)}$ for $0.005 \leqslant \gamma^{(s)} \leqslant 0.01$, and then decreases with increasing $\gamma^{(s)}$ for $0.7 < \gamma^{(s)} \leqslant 1.5$.

(iv) *Low frequency.* The AOSHE S-Mode is a low-frequency mode. The period, $Pe = 2\pi/|kc|$, of the most unstable mode is nearly 1–3 years (Fig. 7b). The period increases with wavenumber k, and decreases with the air–ocean coupling parameter $\gamma^{(s)}$. Such a frequency is on the same order of the ENSO frequency.

(v) *Slow eastward propagation.* The AOSHE S-Mode slowly propagates eastward (Fig. 7c). The phase speed is in the range of 0–1.25 m s^{-1}. For a given $\gamma^{(s)}$, the phase speed decreases monotonically with k, and tends to zero as $k \to \infty$. For $\gamma^{(s)} = 0.01$, the phase speed decreases from 85 cm s^{-1} for $k = 1$ to 12 cm s^{-1} for $k = 5$. For a given k, the phase speed increases monotonically with $\gamma^{(s)}$.

b. *Sensitivity to entrainment parameter* γ_e

The dispersion relation (52) is solved for the eigenvalue D for $\gamma^{(s)} = 0.01$, $\alpha_s^{(s)} = 0.006$, $F = 0.1$, $\epsilon_p = 0.8$, $\lambda = 1$, and for five different values of γ_e: 0.01, 0.05, 0.1, 0.25, 0.5.

Figure 8 demonstrates that the sensitive dependence of γ_e actually contributes to the generation of the low-frequency (interannual) AOSHE S-Mode.

(i) For small values of γ_e ($\gamma_e \leqslant 0.05$) representing a weak entrainment, the growth rate for the AOSHE S-Mode is always negative. This means that the en-

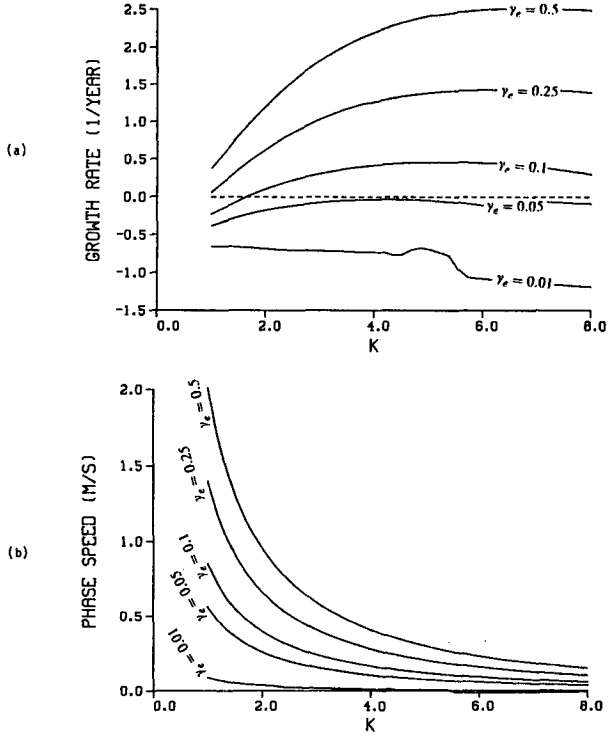

FIG. 8. Dependence of the low-frequency AOSHE S-Mode on the entrainment parameter γ_e: (a) growth rate and (b) phase speed. The other important parameters are $\gamma^{(s)} = 0.01$, $\alpha_s^{(s)} = 0.006$, $F = 0.1$, $\epsilon_p = 0.8$, and $\lambda = 1$.

trainment mixing in the OML should be sufficiently strong to generate unstable modes. For any wavenumber k, the growth rate increases monotonically with γ_e (Fig. 8a). The maximum growth rate of the AOSHE S-Mode increases 0.46 yr^{-1} for $\gamma_e = 0.01$ to 2.5 yr^{-1} for $\gamma_e = 0.5$.

(ii) The AOSHE S-Mode propagates eastward (Fig. 8b). For a given γ_e, the phase speed decreases monotonically with k, and tends to zero as $k \to \infty$. For a given k, the phase speed increases monotonically with γ_e. As $\gamma_e = 0.01$, the phase speed is nearly zero; however, as $\gamma_e = 0.1$, the phase speed reduces from 85 cm s^{-1} at $k = 1$ to 5.8 cm s^{-1} at $k = 8$.

c. *Sensitivity to thermal dissipation coefficient* $\alpha_s^{(s)}$

The dispersion relation (52) is solved for the eigenvalue D for $\gamma^{(s)} = 0.01$, $\gamma_e = 0.1$, $F = 0.1$, $\epsilon_p = 0.8$, $\lambda = 1$, and for five different values of $\alpha_s^{(s)}$: 0, 0.003, 0.006, 0.01, 0.02. Figure 9 indicates the sensitivity of the AOSHE S-Mode growth rate on the thermal dissipation coefficient $\alpha_s^{(s)}$.

(i) For a given wavenumber k, the growth rate decreases monotonically with $\alpha_s^{(s)}$. For $\alpha_s^{(s)} = 0$ (no thermal dissipation in OML), the growth rate is the largest. For $\alpha_s^{(s)} = 0.02$ (approximately 3.3 times the regular thermal dissipation coefficient), there is no unstable mode at all for the whole wavenumber domain.

(ii) The unstable AOSHE S-Mode has length-scale mode selection. The maximum growth rate is located at $k \approx 5$ for all $\alpha_s^{(s)}$. The size of the wavenumber interval for the unstable modes increases as $\alpha_s^{(s)}$ decreases.

A very slight effect of $\alpha_s^{(s)}$ on the AOSHE S-Mode phase speed was found. In the largest scale $k < 3$, the augmentation of the thermal dissipation $\alpha_s^{(w)}$ increases the phase speed by a few percent. In the smaller scale ($k > 3$), there is no effect of $\alpha_s^{(s)}$ on the AOSHE S-Mode phase speed.

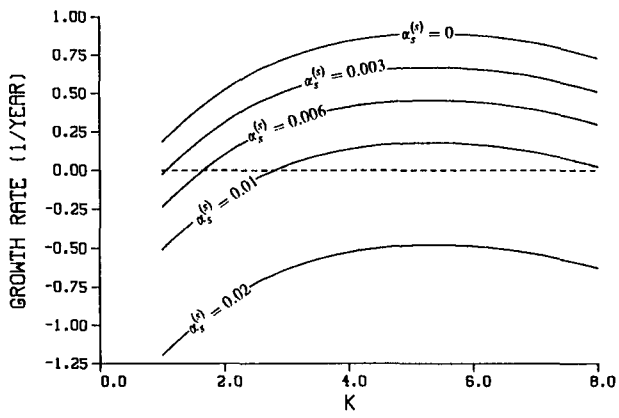

FIG. 9. Dependence of the low-frequency AOSHE S-Mode growth rate on the thermal dissipation parameter $\alpha_s^{(s)}$. The other important parameters are $\gamma^{(s)} = 0.01$, $\gamma_e = 0.1$, $F = 0.1$, $\epsilon_p = 0.8$, and $\lambda = 1$.

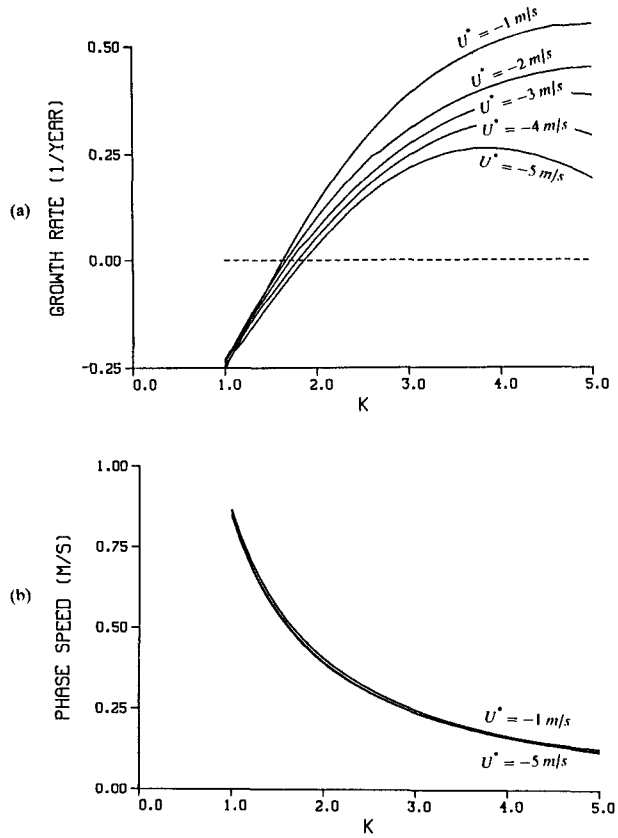

FIG. 10. The dependence of the growth rate (a), and phase velocity (b) of the AOSHE S-Mode on longitudinal wavenumber k for various values of the mean easterlies U^*. The other important parameters are $\gamma^{(s)} = 0.01$, $\gamma_e = 0.1$, $\alpha_s^{(s)} = 0.006$, $\epsilon_p = 0.8$, $\lambda = 1$, and $F = 0.1$.

d. *Sensitivity to mean easterlies* U^*

The dispersion relation (52) is solved for $\gamma^{(s)} = 0.01$, $\gamma_e = 0.1$, $\alpha_s^{(s)} = 0.006$, $F = 0.1$, $\lambda = 1$, $\epsilon_p = 0.8$, and for five different values of U^*: -1 m s^{-1}, -2 m s^{-1}, -3 m s^{-1}, -4 m s^{-1}, and -5 m s^{-1}.

Figure 10 shows the dependence of growth rate and phase speed of the AOSHE S-Mode on k for different values of U^*. It is noticed that the growth rate (Fig. 10a) for a given wavenumber decreases with increasing values of the mean easterlies U^* and that this reduction is enhanced as wavenumber k increases. It is also noticed that the phase speed remains almost the same for different values of the mean easterlies U^*. The reduction of growth rate with the increasing U^* implies that the AOSHE mechanism weakens from the western Pacific to the central and eastern Pacific when OML is in the entrainment regime.

8. Different model sensitivities between AOSHE W and S modes

The different types of sensitivity of AOSHE W and S modes on the model parameters (sections 6 and 7)

are outlined in Tables 3 and 4. Here, the upward arrow ↑ (or downward ↓) indicates the increase (or decrease) of the growth rate (Table 3) or phase speed (Table 4) with the increase of parameters. The parameters (γ, α_s) are ($\gamma^{(w)}$, $\alpha_s^{(w)}$) for the AOSHE W-Mode, and ($\gamma^{(w)}$, $\alpha_s^{(w)}$) for the AOSHE S-Mode.

Three important atmospheric parameters λ, F, and ϵ_p have totally different effects on the growth rate and phase speed of the two AOSHE modes. The increase of F generally represents the enhancement of drag at the ocean surface, $C_D|U^*|$ [see Eq. (26)], which strengthens the TKE generation in OML. More TKE, generated by the surface wind stress, in turn increases the OML depth, which leads to $\partial T_s/\partial t < 0$ in the AOSHE W-Mode, and $\partial T_s/\partial t > 0$ in the AOSHE S-Mode. The two distinct effects of precipitation efficiency ϵ_p on the AOSHE model, augmentation for AOSHE W-Mode and attenuation for AOSHE S-Mode, are also due to the two different kinds of OML-thickness SST feedback. The precipitation brings buoyancy to OML and tends to reduce the OML depth, regardless of whether OML is under weak or strong surface wind forcing. In other words, the precipitation will induce a negative OML depth fluctuation ($h_w < 0$), which causes the two different tendencies for the SST perturbations: $\partial T_s/\partial t > 0$ for a weak surface wind forcing, and $\partial T_s/\partial t < 0$ for a strong surface wind forcing. These two distinct types of SST response have two different effects on the atmospheric convection: enhancement when $\partial T_s/\partial t > 0$ (weak surface wind forcing) and attenuation when $\partial T_s/\partial t < 0$ (strong wind forcing surface).

For the two AOSHE modes, the air–ocean coupling coefficient γ has different effects on growth rate and the same effect on phase speed; however, the OML thermal dissipation coefficient α_s has the same effect on growth rate and different effects on phase speed.

9. Summary

(i) There are two distinct air–ocean feedback mechanisms available for the two different tropical ocean-surface conditions. As the ocean surface is under weak wind forcing, the time-rate change of SST is negatively correlated with OML depth h_w; however, as the ocean surface is under strong wind forcing, the time-rate change of SST is positively correlated with OML depth h_w. Such a difference leads to the generation of two different low-frequency (interannual) modes in the mean easterlies; the eastward-propagating AOSHE S-mode (under strong surface wind forcing) and the westward-propagating AOSHE W-mode (under weak surface wind forcing). This air–ocean feedback mechanism is called an AOSHE mechanism, which might play an important role in the ENSO events.

TABLE 3. Different effects of model parameters on the growth rate of the two AOSHE modes.

AOSHE	γ	α_s	γ_e	λ	F	ϵ_p
W-Mode	↑	↓		↓	↓	↑
S-Mode	Λ-type	↓	↑	↑	↑	↓

TABLE 4. Different effects of model parameters on the phase speed of the two AOSHE modes.

AOSHE	γ	α_s	γ_e	λ	F	ϵ_p
W-Mode	↑	↓		↑	↑	↓
S-Mode	↑	↑	↑	↓	↓	↑

(ii) The AOSHE model predicts the generation of a westward- (or eastward) propagating low-frequency (interannual) mode under weak (or strong) surface wind forcing. By the use of typical values of the parameters for the tropical Pacific, the westward-propagating AOSHE W-mode shows the following features: largest-scale mode selection, faster growth (maximum growth rate is on the order of (2.2 yr^{-1}), low frequency (2–10 year period for the unstable mode), slow westward propagation (phase speed on the order of −20 cm s^{-1}); however, the eastward-propagating AOSHE S-Mode indicates the following properties: wavenumber 3–5 mode selection, slower growth (maximum growth rate on the order of 0.5 yr^{-1}), low frequency (1–3 year period for the most unstable mode), faster eastward propagation (phase speed 10–100 cm s^{-1}).

(iii) The AOSHE mechanism is valid for the whole ocean basin (western, central, and eastern) when OML is in the shallowing regime; however, the AOSHE mechanism weakens from the western Pacific to the central and eastern Pacific when OML is in the entrainment regime.

(iv) Besides the AOSHE W- and S-modes, the AOSHE model preserves the modified WISHE modes. The air–sea feedback effect on the modified WISHE mode is negligible. This indicates that the AOSHE mechanism and the WISHE mechanism are apparently not interfering with each other. The WISHE mechanism is responsible for the generation of the high-frequency mode (30–60 day) in the atmosphere with smallest-scale mode selection; and the AOSHE mechanism is responsible for the production of the low-frequency mode (interannual) with either largest-scale mode selection for the AOSHE W-Mode, or wavenumber 3–5 selection for the AOSHE S-Mode.

(v) In the present study, the advection perturbations are neglected. The system depicts local thermal processes only. There are no large-scale ocean dynamic processes involved. The ocean waves are filtered out in the current AOSHE model. Furthermore, OML with salinity effect is not included here. Combination of the ENSO wave theory and the AOSHE mechanism with consideration of salinity effect will provide a complete

picture of dynamical and thermodynamical interaction between equatorial troposphere and the ocean.

(vi) The AOSHE model can also be served as a linkage between the ocean and the stratosphere since the stratosphere was already included into the WISHE Model in YE91. The inclusion of the stratosphere into the AOSHE model might lead to a possible linkage of the low-frequency oscillations in the ocean and in the stratosphere, such as the quasi-biennial oscillation (QBO).

(vii) The advantage of the equality assumption of subcloud layer and midtropospheric moist entropy fluctuations (8f), is to simplify the model without loss of major physical processes; however, this assumption becomes too strong if one wants to develop a numerical ENSO prediction model including the AOSHE mechanism.

Acknowledgments. I am grateful to K. Emanuel, R. W. Garwood, Jr., R. L. Haney, and K. M. Lau for helpful comments on an earlier version of this paper. The suggestions and comments from J. Nogués-Paegle and two anonymous reviewers are highly appreciated. This work was funded by the National Science Foundation, the Office of Naval Research, and the Naval Postgraduate School.

REFERENCES

Battisti, D. S., 1988: The dynamics and thermodynamics of a warming event in a coupled tropical atmosphere–ocean model. *J. Atmos. Sci.*, **45**, 2889–2919.

——, 1989: On the role of subtropical oceanic Rossby waves during ENSO. *J. Phys. Oceanogr.*, **19**, 551–559.

——, 1991: Reply. *J. Phys. Oceanogr.*, **21**, 461–465.

——, and A. C. Hirst, 1989: Interannual variability in the tropical atmosphere–ocean system: Influence of the basic state, nonlinearity, and ocean geometry. *J. Atmos. Sci.*, **46**, 1687–1712.

Bjerknes, J., 1966: Possible response of the atmospheric Hadley circulation to equatorial anomalies of ocean temperature. *Tellus*, **18**, 820–829.

——, 1969: Atmospheric telecommunications from the equatorial Pacific. *Mon. Wea. Rev.*, **97**, 163–172.

Cane, M. A., and S. E. Zebiak, 1985: A theory for El Niño and the Southern Oscillation. *Science*, **228**, 1085–1087.

——, M. Munnich, and S. E. Zebiak, 1990: A study of self-excited oscillations of the tropical ocean–atmosphere system. Part I: Linear analysis. *J. Atmos. Sci.*, **47**, 1562–1577.

Chu, P. C., and R. W. Garwood, Jr., 1991: On the two-phase thermodynamics of the coupled cloud–ocean mixed layer. *J. Geophys. Res.*, **96**, 3425–3436.

——, ——, and P. Muller, 1990: Unstable and damped modes in coupled ocean mixed layer and cloud models. *J. Mar. Sys.*, **1**, 1–11.

Emanuel, K. A., 1987: An air–sea interaction model of intraseasonal oscillations in the tropics. *J. Atmos. Sci.*, **44**, 2324–2340.

Graham, N. E., and W. B. White, 1991: Comments on "On the role of off-equatorial Rossby waves during ENSO". *J. Phys. Oceanogr.*, **21**, 453–460.

Hirst, A. C., 1986: Unstable and damped equatorial modes in simple coupled atmosphere–ocean models. *J. Atmos. Sci.*, **43**, 606–630.

——, and K. M. Lau, 1990: Intraseasonal and interannual oscillations in coupled ocean–atmosphere models. *J. Climate*, **3**, 713–725.

Hsiung, J., 1986: Mean surface energy fluxes over the global ocean. *J. Geophys. Res.*, **91**, 10 585–10 606.

Kraus, E. B., and J. S. Turner, 1967: A one-dimensional model of the seasonal thermocline. II: The general theory and its consequences. *Tellus*, **19**, 98–106.

Kuo, H. L., 1989: Long-term oscillation in the coupled atmosphere–ocean system and El Niño phenomenon. *J. Climate*, **2**, 1421–1437.

Lau, K. M., and P. H. Chan, 1986: The 40–50 day oscillation and the El Niño/Southern Oscillation. *Bull. Amer. Meteor. Soc.*, **67**, 533–534.

——, and S. Shen, 1988: On the dynamics of intraseasonal oscillations and ENSO. *J. Atmos. Sci.*, **45**, 1781–1797.

McCreary, J. P., 1983: A model of tropical ocean–atmosphere interaction. *Mon. Wea. Rev.*, **111**, 370–387.

——, and D. L. T. Anderson, 1984: A simple model of El Niño and Southern Oscillation. *Mon. Wea. Rev.*, **112**, 934–946.

Meyers, G., 1979: Annual variation in the slope of the 14°C isotherm along the equator in the Pacific Ocean. *J. Phys. Oceanogr.*, **9**, 885–891.

Miller, J. R., 1976: The salinity effect in a mixed layer ocean model. *J. Phys. Oceanogr.*, **6**, 29–35.

Mitchum, G. T. and R. Lukas, 1987: The latitude–frequency structure of Pacific sea level variance. *J. Phys. Oceanogr.*, **17**, 2362–2365.

Neelin, J. D., 1991: The slow sea surface temperature mode and the fast-wave limit: Analytic theory for tropical interannual oscillation and experiments in a hybrid coupled model. *J. Atmos. Sci.*, **48**, 584–606.

Philander, S. G. H., 1985: El Niño and La Niña. *J. Atmos. Sci.*, **42**, 2652–2662.

——, 1990: *El Niño, La Niña, and Southern Oscillation.* Academic Press.

Rennick, M. A., and R. L. Haney, 1986: Stable and unstable air–sea interactions in the equatorial region. *J. Atmos. Sci.*, **43**, 2937–2943.

Riehl, H., 1954: *Tropical Meteorology.* McGraw-Hill, 392 pp.

Schneider, N., and P. Muller, 1990: The meridional and seasonal structures of the mixed layer depth and its diurnal amplitude observed during the Hawaii-to-Tahiti shuttle experiment. *J. Phys. Oceanogr.*, **20**, 1395–1404.

Schopf, P. S., and M. J. Suarez, 1988: Vacillations in a coupled ocean–atmosphere model. *J. Atmos. Sci.*, **45**, 549–566.

Wyrtki, K., 1975: Fluctuations of the dynamic topography in the Pacific Ocean. *J. Phys. Oceanogr.*, **5**, 450–459.

——, 1981: An estimate of equatorial upwelling in the Pacific. *J. Phys. Oceanogr.*, **11**, 1205–1214.

Yamagata, T., 1985: Stability of a simple air–sea coupled model in the tropics. *Coupled Ocean–Atmosphere Models*, J. C. J. Nihoul, Ed., Elsevier, 637–658.

Yano, J. I., and K. Emanuel, 1991: An improved model of the equatorial troposphere and its coupling with the stratosphere. *J. Atmos. Sci.*, **48**, 377–389.

Zebiak, S. E., and M. A. Cane, 1987: A model El Niño–Southern Oscillation. *Mon. Wea. Rev.*, **115**, 2262–2278.